



Cite this: *Chem. Soc. Rev.*, 2024, **53**, 5118

## SERS in 3D cell models: a powerful tool in cancer research

Lara Troncoso-Afonso, <sup>ab</sup> Gail A. Vinnacombe-Willson, <sup>a</sup>  
 Clara García-Astrain <sup>ac</sup> and Luis M. Liz-Márzan <sup>\*acd</sup>

Unraveling the cellular and molecular mechanisms underlying tumoral processes is fundamental for the diagnosis and treatment of cancer. In this regard, three-dimensional (3D) cancer cell models more realistically mimic tumors compared to conventional 2D cell cultures and are more attractive for performing such studies. Nonetheless, the analysis of such architectures is challenging because most available techniques are destructive, resulting in the loss of biochemical information. On the contrary, surface-enhanced Raman spectroscopy (SERS) is a non-invasive analytical tool that can record the structural fingerprint of molecules present in complex biological environments. The implementation of SERS in 3D cancer models can be leveraged to track therapeutics, the production of cancer-related metabolites, different signaling and communication pathways, and to image the different cellular components and structural features. In this review, we highlight recent progress in the use of SERS for the evaluation of cancer diagnosis and therapy in 3D tumoral models. We outline strategies for the delivery and design of SERS tags and shed light on the possibilities this technique offers for studying different cellular processes, through either biosensing or bioimaging modalities. Finally, we address current challenges and future directions, such as overcoming the limitations of SERS and the need for the development of user-friendly and robust data analysis methods. Continued development of SERS 3D bioimaging and biosensing systems, techniques, and analytical strategies, can provide significant contributions for early disease detection, novel cancer therapies, and the realization of patient-tailored medicine.

Received 29th November 2023

DOI: 10.1039/d3cs01049j

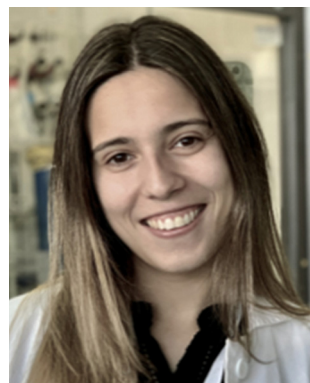
[rsc.li/chem-soc-rev](https://rsc.li/chem-soc-rev)

<sup>a</sup> *BioNanoPlasmonics Laboratory, CIC biomaGUNE, Basque Research and Technology Alliance (BRTA), 20014 Donostia-San Sebastián, Spain.*  
*E-mail: llizmarzan@cicbiomagune.es*

<sup>b</sup> *Department of Applied Chemistry, University of the Basque Country, 20018 Donostia-San Sebastián, Gipuzkoa, Spain*

<sup>c</sup> *Centro de Investigación Biomédica en Red de Bioingeniería Biomateriales, y Nanomedicina (CIBER-BBN), Paseo de Miramón 182, 20014 Donostia-San Sebastián, Spain*

<sup>d</sup> *Ikerbasque Basque Foundation for Science, 48013 Bilbao, Spain*



**Lara Troncoso-Afonso**

where she is involved in the ERC project 4DbioSERS. Her current research is focused on the use of SERS to detect cancer-related biomarkers in 3D cell models.

*Lara Troncoso-Afonso received her B.Sc in Chemistry in 2021 and her M.Sc. in Chemistry at the interface with Biology and Materials Science in 2023, both from the University of Santiago de Compostela. In 2023 she obtained a “FPU” fellowship from the Ministry of Education and Science of Spain, to pursue her PhD and she joined BioNanoPlasmonics group led by Luis Liz-Marzán at CIC biomaGUNE, in Donostia-San Sebastián,*



**Gail A. Vinnacombe-Willson**

*BioNanoPlasmonics group at CIC biomaGUNE in Donostia-San Sebastián, Spain, where she is involved in the European project 4D bioSERS. Her current research includes the development of SERS substrates based on hydrogels for biomedical applications.*

*Dr Gail A. Vinnacombe-Willson received her B.Sc. in Chemistry from the University of San Francisco. She graduated with her PhD in Materials Chemistry from the University of California, Los Angeles, with her thesis on gold nanoparticle patterning and substrate growth. In 2022, she was awarded with the Marie Skłodowska-Curie postdoctoral fellowship for project PLASMO-STEMFATE. She is currently a postdoctoral researcher in the*



# 1. Introduction

Cancer is caused by the uncontrolled proliferation and migration of abnormal cells, resulting in the formation of tumors and spreading to other parts of the body in what we know as metastasis.<sup>1</sup> An ordinary cellular cycle includes growth, mitosis, and apoptosis, but if this cycle is disrupted, cells may start dividing rapidly, eventually leading to tumor formation. Cancer affects millions of people worldwide; in 2020, 18.1 million people were diagnosed, and 10 million people died of this disease.<sup>2</sup> Standard clinical approaches for cancer treatment are surgery, radiotherapy, and chemotherapy. However, surgery is not always feasible, and radiotherapy and chemotherapy are not cell-specific, usually causing unwanted damage to healthy cells and tissues.<sup>3,4</sup> Moreover, the discovery of chemotherapeutic agents takes 10–13 years on average, with only 5% of potential candidates reaching the market.<sup>5</sup>

Tumors are not only composed of tumoral cells but also contain cancer associated fibroblasts (CAFs), endothelial cells, adipocytes, and immune cells (natural killer cells, T cells, B cells, macrophages, *etc.*).<sup>6</sup> All these cellular components are present in the tumor microenvironment and constantly interact with tumor cells, influencing their proliferation, differentiation, migration, decision making, and response to therapeutics.<sup>7</sup> Studying both cell–cell and cell–environment signaling and communication is fundamental in cancer research.<sup>8</sup> Although creating an *in vitro* cell model that considers all the aspects of the tumor microenvironment is difficult, reproducing tumor ecosystems with only a few of the main components may be enough to build more robust models than conventional two-dimensional (2D) monocultures of tumor cells.<sup>9</sup> The limitations of standard 2D cell cultures to reproduce tumoral physiological features are well-known contributors to the high drug development attrition rates.<sup>10</sup> Indeed, to narrow down the translational gap between

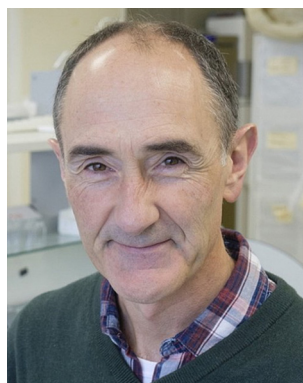
2D cellular models and patients, researchers have placed efforts towards developing reliable three-dimensional (3D) cell models where cancer cells can be cultured in a spatially relevant fashion, together with the components of the tumor microenvironment, to mimic native cell–cell and cell–matrix interactions, as well as their physicochemical and mechanical properties.<sup>11</sup>

Nonetheless, 3D cancer models need to be combined with robust analytical tools capable of imaging these biological constructs and detecting different biomarkers that would regulate cellular behavior, communication, and proliferation.<sup>12</sup> Conventional techniques include flow cytometry, colorimetry, bright field, dark field, or differential interference contrast optical microscopies, as well as scanning or transmission electron microscopies (SEM and TEM, respectively). However, most of them require fixation, sectioning, or destruction of the sample, thereby resulting in loss of biochemical information and presenting a barrier for time-dependent studies.<sup>13</sup> The most intensely used techniques for imaging in biological settings are those based on fluorescence,<sup>14</sup> from conventional wide field and confocal laser scanning fluorescence microscopy, to nonlinear microscopy based on two- or multiphoton absorption, and super resolution techniques such as stimulated emission depletion (STED), stochastic optical reconstruction microscopy (STORM), photo-activated localization microscopy (PALM), *etc.*<sup>15</sup> Despite the usefulness of these techniques for cell imaging, fluorescence-based microscopy is limited by its dependency on either exogenous (chromophores, dyes, quantum dots, *etc.*) or endogenous (cellular autofluorescence) fluorophores, preventing non-fluorescent or weakly fluorescent molecular species to be probed.<sup>16</sup> Moreover, in biological settings some fluorophores might be quenched and suffer from photobleaching.<sup>17</sup> Another issue when using fluorescence in 3D cell models is the limited penetration depth due to poor light transmission through



**Clara García-Astrain**

*Clara García-Astrain is a Juan de la Cierva Incorporación Fellow in the Bionanoplasmonics Lab lead by Prof. Luis M. Liz-Marzán (CICbiomaGUNE, Donostia-San Sebastián, Spain). In 2015 she obtained her PhD from the University of the Basque Country (Donostia-San Sebastián, Spain), after which she completed postdocs at the Institute of Chemistry and Processes for Energy, Environment and Health (ICPEES) from the University of Strasbourg/CNRS (Strasbourg, France) and the Basque Centre for Materials, Applications and Nanostructures (BCMaterials, Leioa, Spain). In 2018, she moved to CICbiomaGUNE where she focuses on the development of polymer nanocomposites for 3D sensing and imaging applications.*



**Luis M. Liz-Marzán**

*Luis Liz-Marzán is an Ikerbasque Professor at CIC biomaGUNE, in San Sebastián (Spain), where he served as the Scientific Director from 2012 to 2021. He obtained a PhD in chemistry from the University of Santiago de Compostela (1992), and after a postdoctoral stay at Utrecht University, he became Professor at the University of Vigo (1995–2012), where he currently holds a part-time professorship. Liz-Marzán has contributed to develop the colloidal synthesis and self-assembly of metal nanocrystals, as well as the characterization and application of their plasmonic properties. His most recent research focuses on various biomedical applications of plasmonic nanostructures.*



non-transparent matrices, such as those present in biological settings.<sup>18</sup>

Thus, studying the components of complex 3D biological models still poses significant challenges and there is a need for continued development of advanced analytical tools that can probe these systems. In this context, Raman spectroscopy is a non-destructive, non-invasive, and label-free technique of growing interest in biophysical and biochemical research.<sup>19</sup> Raman spectroscopy measures (inelastic) light scattering from molecules upon excitation with a highly intense light source. Light scattering is caused by the polarization of the molecular electron cloud under the oscillating electromagnetic field of incident photons, which leaves the molecule in a higher energy state. This process can be explained by considering the formation of a short-lived complex between the photon and the molecule, which is called the virtual state of the molecule. This virtual state is not stable, and the photon is quickly re-emitted as scattered light. In case the molecule retains the same energy and thus the incident and scattered photons have the same frequency, *i.e.*, light is elastically scattered, the phenomenon is known as Rayleigh scattering (Fig. 1A). However, the molecule may also gain or lose energy, so that the scattered photon will have a lower (Stokes) or higher (anti-Stokes) frequency compared to the incident one, so that light is inelastically scattered, which is the basis of Raman scattering (Fig. 1A). The frequency shift of Raman scattered photons can be correlated with the excitation of different molecular vibrational modes, thereby providing information about the molecule's chemical structure. Therefore, Raman scattering is complementary to IR absorption spectroscopy, as both techniques provide a vibrational chemical fingerprint of molecules. However, Raman spectroscopy is of greater interest for biomedical applications due to the high IR absorption but weak scattering by water.<sup>20</sup> However,

the main limitation of Raman spectroscopy is that only one of every  $10^6$ – $10^8$  photons is inelastically scattered, thus requiring longer acquisition times than the dynamic processes occurring inside *in vivo* samples, with their components in constant motion.<sup>21</sup> Moreover, the scattering cross-sections for many metabolites are extremely low, preventing biomarker detection at low concentrations. Fifty years ago, it was discovered that the intensity in Raman measurements can be largely increased when the molecules are in contact with a metallic surface,<sup>22–24</sup> giving rise to a new technique that we know as surface-enhanced Raman Spectroscopy (SERS).<sup>25</sup> This technique has attracted much attention ever since and has been extensively applied in biomedical research.<sup>26</sup>

The surface-enhanced Raman effect occurs when molecules are in close proximity to nanostructured metal surfaces, leading to a significant increase in their Raman scattering intensity, thereby revealing molecular vibrational fingerprints and enabling detection at low concentrations (Fig. 1B and C). This drastic enhancement of the Raman signal stems from a combination of plasmon-assisted amplification of the electromagnetic field (electromagnetic mechanism) and the resonant transfer of electrons between the analyte and the metal (chemical mechanism).<sup>27,28</sup> Plasmonic enhancement of the local electric field is observed in metal particles that have smaller spatial dimensions than the wavelength of incoming light. The interaction of light with metal nanoparticles (NPs) leads to a collective oscillation of the conduction electrons in the metal, which can be resonantly amplified by the incident electromagnetic field, the so-called localized surface plasmon resonance (LSPR).<sup>29,30</sup> In short, the LSPR effect causes an enhancement in the local electric field, altering the polarizability of adsorbed molecules, thereby increasing the efficiency of inelastic scattering events.<sup>31,32</sup> The electromagnetic field can

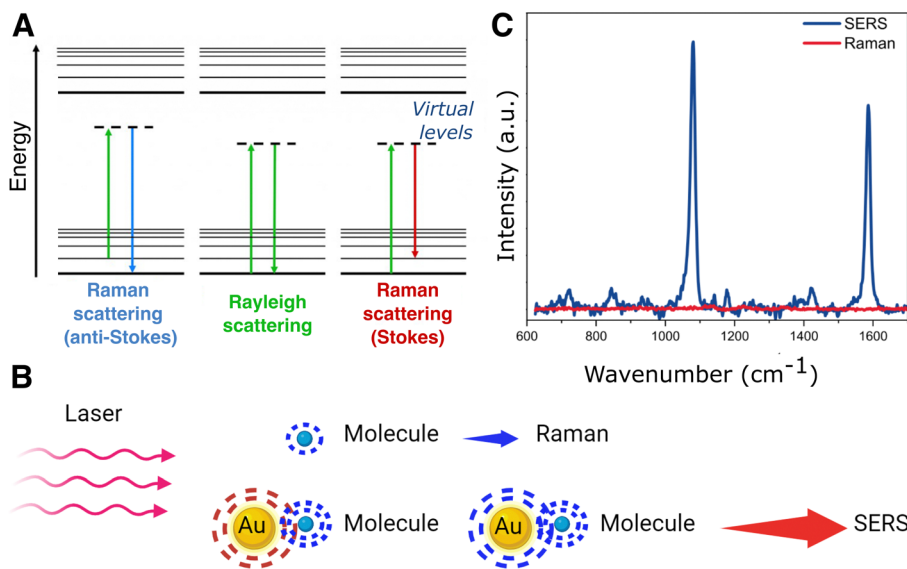


**Fig. 1** (A) Jablonski diagram for scattering processes. (B) Schematic of the surface-enhanced Raman scattering (SERS) principle: a metal nanoparticle is excited with laser irradiation matching the particle's localized surface plasmon resonance. For molecules close to the surface of the nanoparticle, the Raman signal is significantly enhanced. (C) Comparison of SERS and Raman spectra for 4-mercaptobenzoic acid.



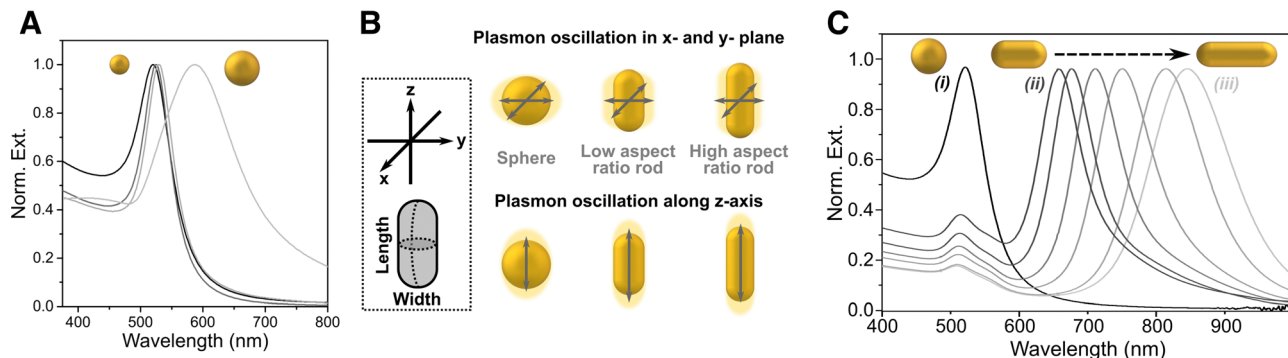


Fig. 2 (A) Extinction spectra for spheres of different sizes. (B) Schematic showing the different plasmon oscillations of an isotropic sphere vs. an anisotropic nanorod. (C) Extinction spectra of gold nanorods with changing aspect ratio. [Adapted from ref. 48].

be further enhanced when confined within short interparticle distances or at sharp NP features, creating regions called “hotspots”.<sup>33–35</sup> The size, morphology, composition and spatial arrangement of the metallic nanostructures are crucial parameters to fine-tune the LSPR and achieve the desired enhancement, as further discussed in Section 3 (Fig. 2). Thus, the pursuit of methods for the preparation of different metallic nanostructures has become a key element to achieve highly reproducible and precise (bio)sensors. Two main fabrication methods are usually distinguished: top-down and bottom-up approaches. Concerning the former, nanolithography is arguably the most popular technique, whereas the latter is usually based on chemical methods for the synthesis of colloidal NPs and their self-assembly into nanostructured substrates. By carefully designing these nanostructures, the local field enhancement can then be leveraged to boost the Raman scattering signal of nearby molecules by up to a factor of  $\sim 10^{14}$  (Fig. 1C).<sup>36–39</sup> SERS can therefore be employed to detect analytes, such as pesticides, cancer therapeutics, and biomarkers, at extremely low concentrations, even down to the single-molecule level.<sup>40</sup> The incorporation of such plasmonic NPs into 3D cell models has been envisaged to allow for the *in situ* detection of biomolecules in the tumoral environment, allowing for real-time, non-invasive monitoring of tumor activity. The combination of SERS and 3D cell models may thus result in a powerful tool for the detection of tumor biomarkers at low concentrations, eventually contributing to the development of more precise and personalized medicine.<sup>41</sup> It is also worth mentioning that, besides cancer research, this technique can be applied to numerous applications in the biomedical field, such as virus<sup>42</sup> and bacteria<sup>43</sup> detection, monitoring of cardiovascular diseases,<sup>44</sup> study of neurodegenerative diseases,<sup>45</sup> monitoring drug delivery,<sup>46</sup> as well as for the development of point-of-care devices for rapid detection of a wide range of biomarkers.<sup>47</sup>

The goal of this review is to discuss the use of SERS in combination with different 3D cell models, to boost cancer diagnosis and treatment. Multicomponent plasmonic systems referred to as “SERS tags” are often applied for both biosensing and bioimaging in 3D. SERS tags (also termed nanotags) are composed of a plasmonic nanoparticle (core), labelled with

so-called “Raman reporters” (RaRs), molecules featuring high Raman scattering cross-sections and affinity for the metal NP surface. Such tags may be subsequently coated with macromolecules such as polymers, lipids, peptides, proteins, or with biorecognition motifs like antibodies or aptamers, to promote different functionalities or target specific biological interactions, leading to a wide variety of configurations depending on the particular application of SERS measurements. In this review, biosensing refers to cases in which the chemical information provided by or encoded to SERS tags is used to detect and/or identify analytes. Additionally, “bare” nanoparticles without RaRs can also provide chemical information *via* “label-free” sensing. Bioimaging refers to instances in which SERS tags are tracked within or around cancer cells and at tumor sites *in vivo*. We thus begin by noting the differences between *in vitro* and *in vivo* 3D cell models, with examples of the various types of models that have been explored. We then cover design rules and describe SERS tags that have been used to interrogate such 3D models. Next, we address how SERS bioimaging can be combined with other techniques to obtain complementary information and higher imaging resolution (multimodal imaging). We also describe the use of “deep” SERS imaging techniques to overcome the limitations of light penetration through opaque materials or those containing many different interfaces/materials, such as tissues. Finally, we discuss the use of SERS for cancer biomarker detection, drug testing, and pH sensing in tumoral environments.

## 2. Three-dimensional cell models

In this section we introduce the main categories of 3D cell models that have been developed so far, aiming to better recapitulate human tumoral environments, compared to 2D cell cultures.

### 2.1. Spheroids

Spheroids result from the self-assembly of substrate-seeded cells, and their formation is driven by cell–cell adhesion forces that are stronger than cell–surface interactions.<sup>49</sup> These 3D structures were first obtained by Moscona *et al.* from organ



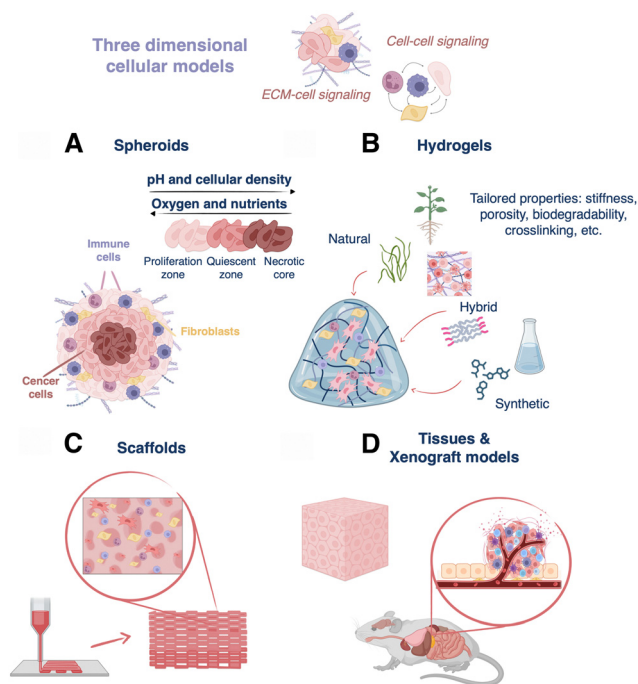


Fig. 3 Diagram describing different 3D cell models: (A) 3D spheroids, (B) hydrogels for cell culture, (C) hydrogel-based 3D printed scaffolds, and (D) tissues and xenograft models.

rudiments of early chick embryo.<sup>50</sup> Nowadays, plenty of methods are available for spheroid formation from single or co-cultures, such as hanging drop<sup>51</sup> or rotating culture,<sup>52</sup> and more sophisticated methods like microfluidics or 3D bioprinting.<sup>53</sup> Spheroids enable studies regarding cell–cell signaling, cell–cell and cell–ECM physical interactions, growth kinetics, gene expression, and drug resistance phenomena.<sup>54</sup> In fact, it has been demonstrated that spheroids are able to mimic the original tissue, for example building hepatocyte spheroids with liver-like functions.<sup>55</sup> In cancer research, spheroids have been extensively used because they can mimic *in vivo* solid tumors, in terms of structural organization and gradients of nutrients, oxygen, and pH, which are established within three-dimensional structures. Multicellular tumor spheroids can be structurally divided into an external proliferating zone, an internal quiescent zone, and a necrotic core (Fig. 3A).<sup>56</sup> Despite the advantages of spheroids, cellular aggregates greater than 1–2 mm in thickness show a limited exchange of nutrients, oxygen, and waste metabolites, resulting in cell death.<sup>57</sup>

## 2.2. Bulk hydrogels

Hydrogels are hydrophilic polymer networks that display great biocompatibility and ability to retain water.<sup>58</sup> These matrices allow the flux of oxygen and nutrients, have similar mechanical properties as those of many soft tissues, and are able to support cell adhesion and protein sequestration.<sup>58</sup> They can be cross-linked *via* chemical (click chemistry, radical reactions, Michael-additions, *etc.*) or physical (thermal, hydrogen bonding, ionic interactions, *etc.*) mechanisms. Moreover, hydrogels can be chemically modified to display particular stiffness, porosity,

ease of functionalization, crosslinking type, biodegradability, and cell compatibility, which are important features to build *in vitro* tissue-like architectures (Fig. 3B).<sup>59</sup> Hydrogel-based 3D cell cultures can be obtained by encapsulating cells within the hydrogel prior to crosslinking or by seeding cells after crosslinking.

Hydrogels can be classified depending on their polymeric origin as natural, synthetic, or hybrid (semi-synthetic). On one hand, natural hydrogels include polysaccharides (chitosan, dextran, *etc.*), proteins/peptides (gelatin, elastin, Matrigel, *etc.*), and decellularized extracellular matrix-based polymeric networks. They are extracted from different biological sources, for instance, collagen, fibrin, and hyaluronic acid are proteins of native ECM, alginate and agarose derive from marine algae, and cellulose is a component of the vegetal cellular wall. In the case of dECM-based hydrogels, they are obtained from decellularized tissue, and thus retain proteins (collagen, fibronectin, laminin, *etc.*), as well as some growth factors and polysaccharides (proteoglycans, glycosaminoglycans, *etc.*).<sup>60</sup> As a result, they reproduce the microstructure, biochemical, and biophysical features of the native tissue, and are able to assist growth and tissue reconstruction.<sup>61</sup> In general, natural hydrogels are biocompatible (low toxicity), bioactive (promote cell activity), and readily available. Nonetheless, their extraction and purification can be expensive, and as natural products, batch-to-batch variability is high, leading to poor reproducibility between different cultures.<sup>62</sup> On the other hand, the group of synthetic hydrogels includes poly(ethylene glycol) (PEG), poly(vinyl alcohol) (PVA), poly(2-hydroxy ethyl methacrylate), poly(glycolic acid), and poly(lactic acid), among others. These polymers display well-defined structures and can be uniformly produced, but they may also restrict cellular functions.<sup>58</sup> Finally, hybrid materials obtained through the combination of synthetic and natural polymers are a third option.<sup>63</sup> These composites combine the properties of both polymer types and can be designed to mimic the biophysical and biochemical features of the natural extracellular matrix.<sup>64</sup> In any case, the choice of one or another possibility finally relies on the particularities of the cell culture and the type of targeted tissue or tumor. Different combinations of hydrogels for cell culture are subsequently addressed in Section 3.3.

## 2.3. Scaffolds

Scaffolds are constructs designed to support cell growth outside of the body, trying to reproduce the extracellular microenvironment. These 3D structures should display biocompatibility, reproducibility, high porosity, pre-designed biodegradability, as well as suitable mechanical and biochemical properties to promote cell attachment, proliferation, and migration.<sup>65</sup> Over the past decade, many materials such as metals (orthopedics), ceramics (implants), and polymers (tissue engineering), have been used to prepare scaffolds for biomedical applications.<sup>52</sup> Focusing here on polymers, hydrogel-based scaffolds are of particular interest because of the properties described in Section 2.2 above. Different methods can be used to build up hydrogel-based scaffolds, ranging from classical templating to



more sophisticated 3D printing,<sup>66</sup> which enables the construction of multiscale architectures by precise deposition of materials in *x*, *y*, and *z* directions. Three primary 3D printing techniques can be mentioned: extrusion, laser-assisted, and inkjet printing.<sup>67</sup> Hydrogels can be used as inks because they are viscoelastic polymers with non-Newtonian properties, allowing for extrusion from a nozzle to yield a controlled deposition of filaments.<sup>68</sup> In addition, low-viscosity hydrogels can be combined with cells, resulting in specialized bioinks that can be used to accurately position cells within the scaffold.<sup>69</sup> Otherwise, cells can be seeded and cultured directly on top of the hydrogel-based scaffold post-printing, allowing them to grow and proliferate with the scaffold support.<sup>70–72</sup> In short, these complex structures display high resolution in all spatial dimensions and tunable biochemical, biophysical, and mechanical properties for the reliable and reproducible production of 3D cell models (Fig. 3C).

#### 2.4. Xenograft models and tissues

Tissues represent another common 3D model, which can be studied *in vivo* in live animals and/or *ex vivo* as cultured or resected tissue (Fig. 3D). Although human tissues can be cultured *ex vivo*, they require the use of dynamic bioreactor setups and culture over several days (even up to 60 days).<sup>73</sup> Thus, as an alternative for *ex vivo* studies, porcine tissues and organs are relatively easy to obtain, while being compositionally similar to human tissues.<sup>74</sup> *In vivo*, immunocompromised or humanized mice and rats implanted with human cancer cells are the most common models. In general, the design of biologically accurate cancer models is challenging because oncogenesis results from genetic and epigenetic anomalies that arise and evolve uniquely patient-to-patient, and tissue inhomogeneities exist, even within the same tumor.<sup>75,76</sup> This is why, although many studies are based on implementing tumors from immortal cancer cell lines in xenograft models (especially because they are relatively easy to engraft/obtain), patient-derived xenografts (PDX) are also gaining traction as 3D *in vivo* models.<sup>75,77</sup> However, PDX models also have their limitations, for example, the surrounding ECM, cells, vasculature, *etc.* – the so-called “tumor stroma” – in animal models is not the same as that of the primary tumor, and accurately replicating the stroma is challenging.<sup>78,79</sup> Moreover, the body size, anatomy, physiology and pathophysiology of rodents differs significantly from those in humans, and when immunocompromised animals are used, limitations arise in the conclusions that can be drawn from drug resistance studies.<sup>5,80,81</sup> With PDX models, one also faces the challenge that engraftment success rate can vary wildly, often leading to the loss of difficult-to-obtain patient-derived samples.<sup>82</sup> Ultimately, these drawbacks have promoted research interest in human tissue engineering.<sup>83</sup> However, until now, owing to their high engraftment success rates with commercial cell lines and their ability to replicate tumor microenvironments with good fidelity, xenograft models have enabled significant developments in the design and implementation of SERS probes in 3D, which will be discussed further in Sections 3 and 4.

### 3. Designing SERS tags for three-dimensional cell models

Naturally, the composition, concentration, and geometry of the plasmonic NP units plays a significant role in determining the biocompatibility, scattering intensity, and measurement conditions. Metals with plasmonic responses in the ultraviolet (UV)-visible-near infrared (NIR) spectral range include gold, silver, copper, and aluminum but, to date, primarily silver and gold have found applications in biological environments.<sup>84</sup> Gold and silver NPs (AuNPs and AgNPs, respectively) display large optical cross sections, can be readily bio-functionalized, and their optical response can be tailored – through NP size and shape – across the visible and NIR regions of the electromagnetic spectrum.<sup>85</sup> The ability to tune the LSPR wavelength in the NIR is key for matching the “biological transparency windows” where there is maximum penetration of light and minimum tissue autofluorescence and photodamage. Even though AgNPs provide higher field enhancements and stronger SERS activity, they can be cytotoxic and are prone to degradation *via* oxidation and sulfidation.<sup>86–88</sup> However, these negative properties can be mitigated in certain configurations, and relevant strategies will be discussed in the following section. Compared to AgNPs, AuNPs have higher biocompatibility and stability against oxidation, rendering them the preferred choice for incorporation in 3D cell models.<sup>89</sup> Gold nanostars (AuNSts), nanoshells, nanoprisms, and nanorods (AuNRs) can exhibit LSPR modes in the NIR.<sup>90–93</sup> Even though AuNPs are particularly stable compared to other plasmonic metals, some precautions still need to be taken to prevent reshaping when using geometries with sharp features.<sup>94</sup>

Beyond the SERS tags themselves, measurement parameters such as acquisition time, laser wavelength, power density, *etc.*, must be carefully optimized for biological studies to ensure cell viability. Tuning measurement conditions is important because the common geometries used in SERS (nanostars, nanoshells, and nanorods) can efficiently generate localized heat in response to NIR irradiation,<sup>95–97</sup> which may damage or alter the behavior of cells or biological systems under study.<sup>98</sup> Cellular homeostasis takes place between 37 and 41 °C, and higher temperatures closer to ~48 °C cause the tertiary structure of proteins to be disrupted, a process that becomes irreversible above ~50 °C.<sup>99</sup> Depending on the size, shape, and configuration of the metallic nanostructures and the irradiation conditions, it is possible to reach temperatures higher than 100 °C at the nanoscale.<sup>95,97</sup> Therefore, the laser energy delivered to NP-labelled cells must be controlled to avoid laser-induced (photo)toxicity while providing a reliable SERS signal.<sup>98</sup> Therefore, the optimization of several imaging parameters is required to maintain cell viability in 3D systems. Irradiation time and repeated exposure of cells to the laser beam are important factors to bear in mind, low laser power and/or fast acquisition times being optimal. Alternatively, off-resonance Raman, whereby laser irradiation wavelengths are mismatched with the LSPR, can also prevent photothermal damage, which has been applied for SERS studies on tissues.<sup>100</sup>



Altogether, careful control over spectral acquisition parameters is essential, and a number of considerations are to be made in the design of the tag itself, as will be further discussed in Subsection 3.1. In the following subsections (3.2–3.4), we will discuss strategies for incorporating plasmonic nanotags into different types of 3D models.

### 3.1. SERS labelling for sensing and imaging

Generally, to effectively monitor the spatial and temporal distribution of distinct cell populations, it is necessary to employ labelling strategies, such as fluorescence or radioactivity, among other examples.<sup>101</sup> In the case of SERS imaging, decoration of the surface of plasmonic NPs with different RaRs results in a variety of SERS tags that can be used to track cells upon internalization (Fig. 4). The purpose of this section is to provide

a concise overview of various SERS labelling options; for more comprehensive information regarding SERS nanotag configuration, readers are referred to recently published reviews.<sup>102</sup>

Overall, the designed SERS tags must be biocompatible and stable under biologically relevant conditions.<sup>102</sup> Therefore, after RaR adsorption, an external coating is usually deposited to improve their stability and biocompatibility, and to modulate intracellular uptake (Fig. 4A). The application of this coating holds significance in preventing RaR leakage, safeguarding against SERS signal contamination from other interfering molecules, mitigating the potential toxicity of NPs, and minimizing unintended intensity fluctuations resulting from plasmon coupling induced by particle–particle interactions. Commonly employed encapsulation strategies include different types of coatings made of peptides or proteins,<sup>103,104</sup>

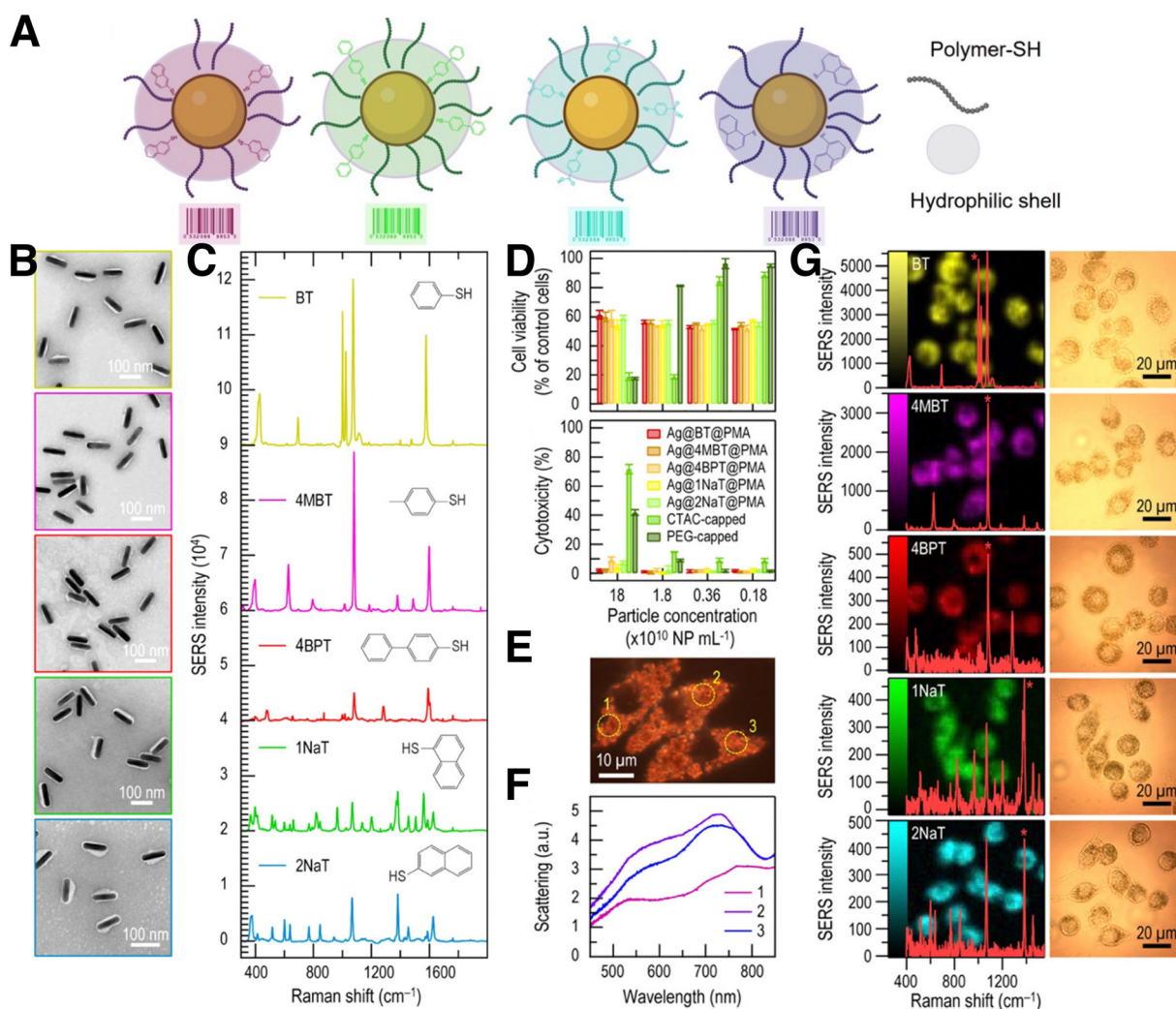


**Fig. 4** (A) Schematic view of SERS tags comprising a metal NP core functionalized with the selected Raman reporter and a thiol-binding polymer, and further stabilized with an amphiphilic polymeric shell. (B) TEM images of silver nanorods (AgNRs) coated with PMA and functionalized with five different RaRs. From top to bottom: benzenethiol (BT), 4-methyl benzenethiol (4-MBT), 4-BPT, 1-NaT, 2-NaT. (C) Corresponding SERS spectra of the samples in B. (D) Cell viability and cytotoxicity results of AgNRs incubated with J774 macrophage cells, from MTT and LDH viability assays, respectively. (E) Real-color dark-field scattering image and (F) dark-field scattering spectra measured from three individual J774 cells containing AgNRs functionalized with BT. (G) SERS images measured from J774 cells containing AuNRs with different RaRs and their corresponding spectra (left) and bright field images of the cells (right). [Adapted with permission from ref. 110 Copyright (2020) American Chemical Society]



liposomes,<sup>105</sup> silica,<sup>106</sup> or polymers.<sup>107,108</sup> The choice of coating should be determined by the final application, considering factors such as biodegradability, long-term stability, agglomeration, binding competition, *etc.* As an example, coatings based on amphiphilic polymers, such as dodecylamine-modified polyisobutylene-*alt*-maleic polymer (PMA), have been demonstrated to improve the stability of SERS tags over extended periods of time.<sup>108</sup> In this system, NP internalization can be enhanced through an additional coating step with a cationic polymer such as poly-L-arginine hydrochloride (PA), because cellular uptake is known to be enhanced for positively charged NPs.<sup>107</sup>

Whereas most NPs used for SERS cell labelling relate to anisotropic structures featuring plasmon resonances in the NIR region, synthetic strategies can also be implemented to fine-tune the aggregation of spherical AuNPs and redshift their plasmon resonances through plasmon coupling. To this end, the ligand ratio between RaRs and stabilizing polymer layer can be tuned to control NP aggregation. For example, the use of poly(isoprene)-diethylenetriamine (PI-DETA) as NP ligand and poly(isoprene)-*block*-poly(ethylene glycol) (PI-*b*-PEG) as a biocompatible micelle builder, combined with a solvent-induced self-assembly process, has been reported to encapsulate AuNP clusters. The number of encapsulated particles can be adjusted by varying the PI-*b*-PEG to PI-DETA ratio, and the particles can be labelled with RaR molecules.<sup>109</sup> Pre-labelling of individual NPs with RaRs appears to be more effective than RaR incorporation into the assemblies, to ultimately introduce them into the resulting hotspots. In this case, PI-DETA was partially replaced by RaRs, resulting in a less dense ligand shell with

NPs in closer proximity. Therefore, the type of RaR and the number of incorporated molecules will influence NP aggregation and should be addressed carefully. Enhancement factors of  $10^4$ – $10^5$  were reported for these systems, with tunable LSPR depending on parameters such as incubation time and RaR content.<sup>109</sup>

Although most reported systems for SERS bioimaging rely on AuNPs, due to their well-known biocompatibility, silver-containing NPs can also be protected from external conditions by means of appropriate synthetic protocols, to prevent oxidation. Zhuo *et al.* reported the codification of monodisperse Ag nanorods (AgNRs) with up to five different RaRs, for intracellular SERS imaging (Fig. 4B–G). As mentioned above, the unique dielectric properties of Ag are hindered by its high cytotoxicity and poor stability in biological settings. However, as previously reported for AuNRs, PMA can be also used to coat and stabilize AgNPs. PMA-coated Au@Ag nanorods derived from Au bipyramids were reported to be stable, non-cytotoxic, and biocompatible, as well as suitable for SERS imaging of J774 macrophages, upon labelling with various RaRs.<sup>110</sup>

Another interesting feature of SERS tags is related to multiplexing, owing to narrow SERS peaks and the possibility of pre-labelling different cell populations with different SERS tags and relocating the tagged cells in a mixed co-culture *via* simultaneous excitation with a single laser source.<sup>98</sup> Multiplex imaging based on SERS tags conjugated to antibodies or aptamers designed for active cell targeting can also be useful for imaging distinct cell types within mixed cultures (Fig. 5). In one example, Nima *et al.* employed up to four different RaR molecules; 4-mercaptobenzoic acid (4-MBA), 4-aminothiophenol (4-ATP),

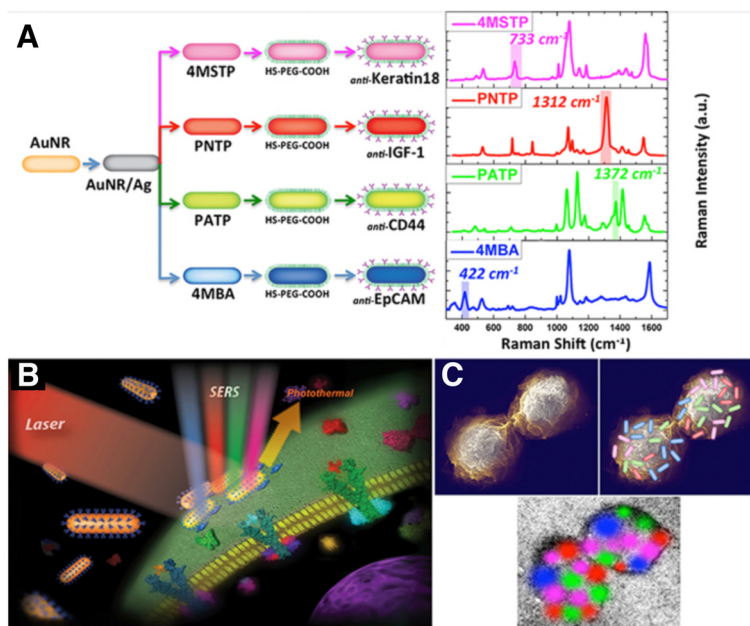


**Fig. 5** (A) Scheme showing four types of nanotags functionalized with different antibodies and their corresponding SERS spectra. Non-overlapping peaks from each SERS spectrum were assigned a different color, as indicated: 4MBA/anti-EpCAM (blue), 4-NTP/anti-IGF-1 (red), 4-ATP/anti-CD44 (green), 4-MSTP/anti-Keratin18 (magenta). Schemes showing proposed (B) breast cancer cell surface targeting by SERS tags and (C) multi-color 2D spatial distribution of SERS intensities, showing how the tags can assist in mapping the cell surface. [Reproduced from ref. 111 with permission from Springer Nature].





4-nitrothiophenol (4-NTP) and 4-(methylsulfanyl) thiophenol (4-MSTP), linked to four breast cancer markers (anti-epithelial cell adhesion molecule, anti-CD44, anti-keratin, and anti-insulin-like growth factor antigen) for the detection of circulating tumor cells.<sup>111</sup> With this approach, the specificity of the detection of a particular cell type can be enhanced, reducing the number of false readings. The identification of human epidermal growth factor receptor 2 (HER2)-positive breast cancer cells has also been possible by SERS imaging.<sup>112</sup> Anti-HER2 antibody-conjugated AuNPs were prepared to target breast cancer cells using 4-MBA as both RaR and conjugation site for attaching antibodies.<sup>112</sup> Following this strategy, it was possible to distinguish between HER2-positive and HER2-negative expressing cells, according to differences in SERS signal intensity. SERS tag labelling can also be used to distinguish between cancerous and healthy cell lines. In an example, Rodal-Cedeira *et al.* reported the bioconjugation of nanocapsules with antibodies against three different cell surface receptors epidermal growth factor receptor (EGFR), epithelial cell adhesion molecule (EpCAM), and CD44.<sup>113</sup> SERS detection was carried out simultaneously in a co-culture of human epithelial carcinoma A431 cell line and nontumoral murine fibroblasts 3T3 2.2. cells. The results showed that 3T3 2.2 cell line only expressed CD44, whereas A431 cells expressed all three antibodies, demonstrating the ability of the SERS tags to distinguish between both cell populations.

### 3.2. Implementing SERS tags in spheroids

Incorporation of SERS tags in spheroids can be accomplished through two main methods: prior internalization into individual cells or post penetration from the periphery into the spheroid core. Cell internalization is determined by the ability of a SERS tag or biofunctionalized NPs (without RaRs) to travel through the plasma membrane, whereas post-penetration depends on the system's diffusion through interstitial spaces, with size, geometry, and surface charge being the most relevant parameters in both cases.<sup>114–116</sup> Sujai and co-workers compared the internalization efficiency of neutral, positively and negatively charged AuNPs, functionalized with 2-(4-methylthiobenzylideneammononitrile), within 2D HeLa cell cultures and multi-layered HeLa spheroids.<sup>117</sup> Their results demonstrated greater internalization of positively charged NPs in the 2D HeLa cell cultures, where negatively charged particles had a higher penetration into the core of the spheroids. Similarly, McCabe *et al.* compared NP localization in 2D glioblastoma U87-MG cell cultures and spheroids.<sup>118</sup> Gold NPs functionalized with (4-1H-pyrazol-4-yl) pyridine were encapsulated in a silica shell, then tenascin-C antibody was immobilized on the tags to target U87-MG glioblastoma cells which overexpress tenascin-C protein. Although the antibody labelled-NPs were found throughout the whole cell in U87-MG monolayer culture, they were shown to accumulate in the spheroid periphery. The authors identified the larger size of the particle, with a diameter > 30 nm being optimal for spheroid penetration, and the blocking of active transport processes due to a lack of nutrients and oxygen in the spheroid core, as the cause of this result.<sup>119</sup>

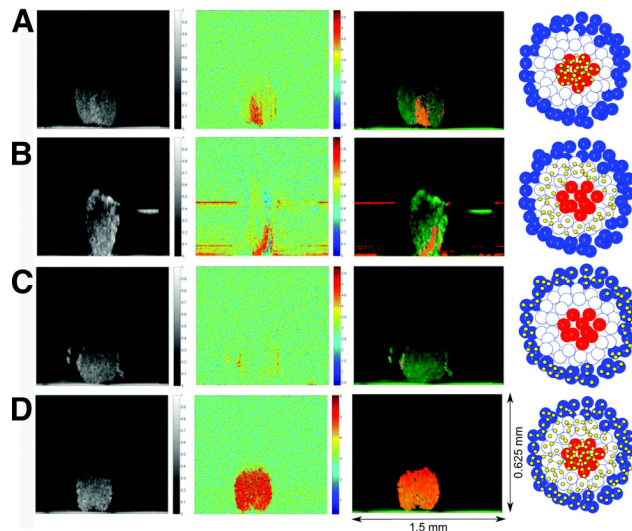


Fig. 6 Photothermal optical coherence tomographs showing SERS nanosensors in the core, intermediate, and outer zones of a spheroid. Optical coherence tomograph (left column), photothermal image (central left column), overlay of both (central right column), and schematic representation (right column) of (A) gold nanoshells in the interior, (B) intermediate part, and (C) outer part, and (D) throughout the spheroid. [Reproduced from ref. 120 with permission from the Royal Society of Chemistry].

Aside from the size and charge of the SERS tags, incubation method and time can also affect their final localization in the spheroid structure. Jamieson *et al.* fabricated multicellular tumor spheroids, then performed incubations with SERS tags either in 2D cell culture before spheroid formation or with RaR-labelled nanoshells at different time points during spheroid formation (Fig. 6).<sup>120</sup> This approach resulted in spheroids with SERS tags either in the core (Fig. 6A), intermediate area (Fig. 6B), outer zones (Fig. 6C), or throughout the spheroid (Fig. 6D). Drug treatment of MCF-7 and PC3 spheroids was studied by monitoring the SERS spectra of the RaRs, 4-MBA, naphthoquinone, and methyl-naphthoquinone, present on the tags, from which pH and redox potential gradients could also be determined. In summary, the type of cells involved, the spheroid building method and the morphological (size, charge, and coating) characteristics of AuNPs are of great importance for SERS sensing and imaging in these 3D models.<sup>121</sup> Thus, all parameters must be carefully chosen to maintain viability and achieve efficient internalization and sensing/imaging throughout spheroids based on different cell lines.<sup>122</sup>

### 3.3. Fabrication of plasmonic-hydrogel hybrid materials

Bulk hydrogels can be combined with plasmonic NPs to turn the resulting composite into a SERS substrate for biodetection. The incorporation of either SERS tags or bare metal NPs (either to be subsequently functionalized with RaRs or applied for label-free sensing) within hydrogel-based matrices has been reported for various metals, resulting in nanocomposites with applications in drug delivery, as bioactive implants, and stimuli-responsive materials for tissue engineering.<sup>123</sup> In fact, bulk hydrogels containing plasmonic NPs can serve both as



SERS substrates and as plasmonic inks to 3D print scaffolds in which cells can be cultured and monitored.

Among the various synthesis protocols for hydrogel-NP composites we highlight the following common approaches: (a) hydrogel formation in NP suspension; (b) NP embedding into the hydrogels after gelation; (c) *in situ* formation of NPs within the gel; and (d) the use of NPs as crosslinking agents.<sup>124</sup> In general, the rheological (yield stress, shear stress, storage and loss modulus, *etc.*) and physicochemical (response to temperature, swelling, hydrophobicity, *etc.*) properties of the hydrogel, as well as the optical (absorption, scattering, reflection, emission, *etc.*) properties of the NPs, may differ compared to those of the resulting composite.<sup>125,126</sup> The study carried out by García-Astrain *et al.* assessed shear thinning, yield point, and viscoelastic modulus for a mixture of HAMA and  $\kappa$ -carrageenan polymers, containing either bare or PEG-coated AuNRs or AuNSts.<sup>71</sup> The effect of NP concentration was interrogated, which was found not to affect the shear thinning, but was determined to alter the storage modulus ( $G'$ ), which was shown to increase with the addition of up to 0.5 mM of  $[Au^0]$ , then decreasing for higher concentrations. Despite these changes to the physical properties of the gel, the resulting composite was successfully used as an ink for printing high resolution scaffolds (as described in Section 2.3) with 250  $\mu$ m interlinear spacing, which could be applied for biosensing (see Section 5.1). In summary, the viscoelastic properties of plasmonic hydrogels can be tailored by selection of the hydrogel component, NP type, concentration, and functionalization.

Most often, plasmonic NPs are mixed with the hydrogel prior to constructing the scaffold as in the previous example (Fig. 7A), but the formation of NPs *in situ*, i.e., within the gel, has also been explored (Fig. 7B). As another example of the former, Plou *et al.* described the fabrication of SERS active 3D printed scaffolds using a bioink containing gelatin, alginate and AuNRs.<sup>72</sup> Regarding the latter approach, Lehman and

colleagues built plasmonic Au/pHEMA composite scaffolds by including gold NP precursor ( $Au^{3+}$ ) in a pHEMA matrix and then incubating in sodium ascorbate solution, after the polymer was cured with UV-light, to form NPs *in situ*. By following this protocol, the authors aimed to prevent AuNP aggregation during processing and 3D printing.<sup>127</sup> However, the chemicals used for gold reduction can also react with the hydrogel and the resulting material might contain potentially cytotoxic unreacted chemical species or reaction by-products, which would hinder the use of these scaffolds for 3D cell culture.<sup>128</sup>

#### 3.4. Integrating SERS tags in tissues

SERS tags can be incorporated into tissues *ex vivo* by either direct injection,<sup>129</sup> placing a tissue slice on a SERS substrate,<sup>130</sup> or by enclosing a chamber containing SERS tags within the tissue.<sup>131,132</sup> For *in vivo* 3D SERS studies related to cancer, rodent xenograft models are common, as described in Section 2.4. While the earliest example of *in vivo* SERS biosensing from the group of Van Duyne applied a plasmonic substrate implanted in rats, the use of colloidal NPs is currently seen as a requirement to extend the imaging/sensing capabilities beyond 2D.<sup>41,102,133</sup> In some studies, colloidal nanotags are delivered by direct subcutaneous, muscular, or ( $\sim 1$  cm) deep muscular injection,<sup>134</sup> but it is also possible to “passively” deliver the SERS tags to tumor sites *via* intravenous injection, thanks to the so-called enhanced permeation and retention (EPR) effect, *i.e.*, the tendency of NPs to accumulate in tissues with high vascular permeability (*e.g.*, tumors).<sup>135,136</sup> In this sense, NPs with sizes of 5–200 nm have been reported for “passive” tumor targeting because both smaller and larger NPs are cleared through either the kidney or the mononuclear phagocyte system.<sup>137</sup> Alternatively, “active” targeting using antibodies, aptamers, or other ligands, may enhance the accumulation of plasmonic tags introduced intravenously at selected tumor regions, which can be helpful both as a diagnostic tool and for further increasing the SERS signal at the target site.<sup>102,103,109,138–140</sup>

## 4. SERS bioimaging in 3D cell models

McAughtrie *et al.* reported for the first time the combination of Raman and SERS for 3D cell imaging, with the aim of simultaneously performing multiple component detection and confirming NP internalization, without requiring additional intracellular imaging techniques, such as TEM.<sup>141</sup> 3D cell mapping with Raman spectroscopy was combined with SERS mapping to confirm the localization of the SERS tags in the interior of Chinese hamster ovarian cells. Silver citrate-capped NPs were coated with four different RaRs, 4-mercaptopyridine (4-Mpy), 5'-dithiobis(2-nitrobenzoic acid) (DTNB), 4-nitrobenzenethiol (NBT) and 2-naphthalenethiol (2-NAT), then NP aggregation was induced by adding 1,6-hexamethylenediamine to produce hotspots. Finally, poly(vinylpyrrolidone) (PVP) was added as quencher for hot spot stabilization. The SERS tags were later delivered to the cells and volume mapping was

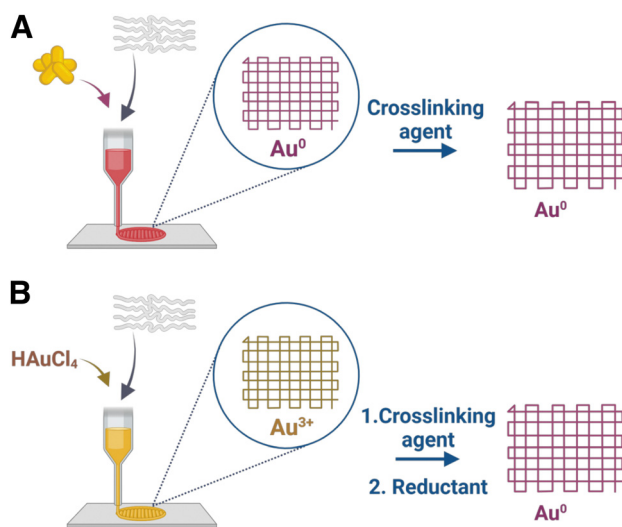


Fig. 7 Scheme for 3D printing of plasmonic scaffolds, using (A) hybrid bioinks comprising NP colloids and hydrogels, or (B) hybrid bioinks made from chemical precursors and hydrogels.



performed by collection of Raman and SERS images with 0.5 mm resolution in *x*- and *y*-directions, and 1 mm resolution in the *z*-direction. The authors were able to identify three out of the four tags intracellularly. A certain degree of colocalization was reported due to their simultaneous administration to the cells, but the tags did not contain any functionalities to target specific subcellular regions.

The uptake and distribution of NPs within cells might also change over time. Here again, SERS imaging can be used as a non-invasive tool, to estimate *in situ* the number of particles remaining in cells over time, through a correlation between signal intensity and number of SERS tags. Lenzi *et al.* evaluated the average SERS intensity per NP by using correlated TEM and SERS.<sup>142</sup> AuNSts and AuNRs with four different RaRs (4-methyl benzenethiol (4-MBT), benzenethiol (BT), 2-NAT and 4-bisphenilthiol (4-BPT)) were applied to develop an application software (SERSTEM App), that can be used for the correlation.

One of the advantages that SERS offers over fluorescence microscopy is the possibility to perform simultaneous SERS imaging and sensing. In this way, 3D cell maps of SERS tags and cell biomarkers can be achieved simultaneously to provide information regarding their spatiotemporal distribution. Chen *et al.* reported the use of labelled and label-free SERS for 3D HeLa cell imaging, using spherical gold NPs labelled with 4-MBA, crystal violet, and crystal violet acetate. For the incorporation of these three dyes, a poly-allylamine (PAH) shell was incorporated onto the NPs to reduce aggregation. The PAH shell also introduced  $-NH_2$  groups on the NP surface that could be used for subsequent functionalization.<sup>143</sup>

#### 4.1. *In vitro* SERS bioimaging

Although only few studies have reported the use of SERS imaging in 3D, this field is undergoing significant expansion. SERS imaging has been used to study the differences of NP uptake between 2D cell monolayers and 3D cell models, which eventually provides information about the possible mechanisms behind NP internalization and diffusion, which depend on the RaR composition/charge and NP size and geometry, as discussed in Section 3.2.<sup>117,118</sup> In one example, Liu *et al.* designed SERS tags with different sizes, each coated with a particular RaR (34 nm – Au@MBA@Ag; 60 nm – Au@4-mercaptinitrobenzoic acid (MNBA)@Ag; 108 nm – Au@2,3,5,6-tetrafluoro-4-mercaptobenzoic acid (TFMBA)@Ag; 147 nm – Au@4-mercaptopyridine(MPy)@Ag) to compare their accumulation in T47D human breast cancer multicellular spheroids (Fig. 8A).<sup>144</sup> The highest degree of internalization and diffusion across interstitial spaces was ultimately achieved for the 60 nm Au@MNBA@Ag NPs (Fig. 8B and C).<sup>145,146</sup> This result is consistent with other uptake studies (albeit not performed in spheroids), which found that NPs with dimensions close to 50 nm more efficiently penetrate into cells by endocytosis. It has been suggested that the binding of single nanoparticles with diameters much smaller than 50 nm is not energetically favorable and that the membrane encapsulation process for particles much larger than 50 nm is kinetically disfavored.

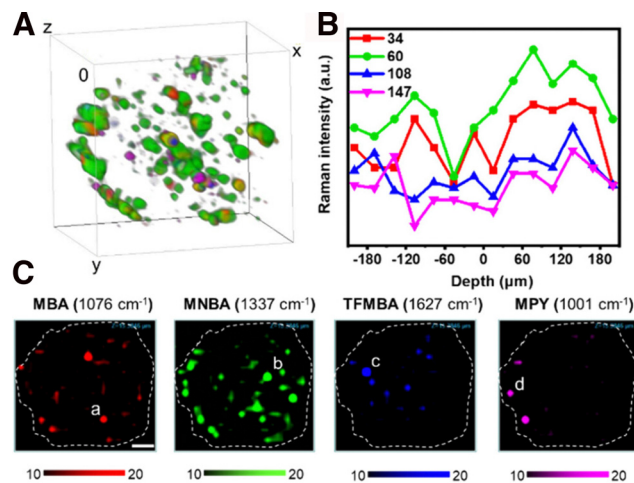


Fig. 8 (A) Reconstruction of a T47D spheroid using the SERS intensities from four SERS tags (color code provided in C). (B) Average SERS intensity from 34, 60, 108, and 147 nm NPs in each layer. (C) Individual SERS mapping channels of the spheroid with RaRs [Adapted with permission from ref. 144 Copyright (2023) American Chemical Society].

Instead of using labels, the spectral bands associated with different biomolecules ubiquitously present in cells can be used to image nucleic acid, lipid, and protein-rich regions. Pan and co-workers reported the synthesis of silver nanowires at the tip of a carbon nanoelectrode, for recording spectral data at various penetration depths in MCF7 breast cancer spheroids *via* direct insertion.<sup>147</sup> The different spectral bands were attributed to lipids, proteins, phospholipids, and nucleic acids, and their distribution was imaged at different regions of the spheroid (cellular wall, interstitial spaces, *etc.*). More recently, the same group reported the use of this setup to determine intracellular and extracellular pH.<sup>148</sup>

Besides single cells or cell clusters, SERS imaging has been recently implemented in 3D substrates, such as polymers or tissues, thereby expanding the applications of SERS bioimaging to more complex 3D cell models. Vantasin *et al.* reported the incorporation of octahedral silver hexapod microparticles labelled with the RaR 4-ATP, into layered matrices containing different polymer components.<sup>149</sup> The microparticles were mixed into blended and layered polymer systems, and inhomogeneities in the materials were identified with 3D SERS mapping. Overall, these results support the importance of polymer composition, assembly, and transparency for designing complex 3D scaffolds for SERS imaging.

Another example of 3D SERS imaging was reported by Jimenez de Aberasturi *et al.*, where a 3D cell culture model was used, comprising unlabeled and SERS tag-labeled fibroblasts, in a layer-by-layer system.<sup>107</sup> In this work, AuNSts and AuNRs were encoded with 4-BPT and 2-NAT, respectively, or labelled with fluorescent dyes. Signal overlap was avoided by using layers of unlabeled cells and Pearson's correlation coefficients were employed for linear correlation with the corresponding reference spectrum. This complex 3D sample was imaged with 5  $\mu$ m resolution in *x*, *y*, and *z*, and a well-defined layered structure could be observed within an area of



$10^4 \text{ mm}^2$  in  $x$  and  $y$ . Due to the instrument configuration, the measurements were carried out from the top to the bottom layers, resulting in a lower definition of the 3D map toward the bottom of the sample and the need for data processing to enhance the signal-to-noise ratio. Therefore, the visualization of living organisms relies on the development of compatible 3D model configurations that improve the sensitivity and specificity of the technique. Measurement setups and acquisition times should also be compatible with biological samples. Additionally, there is a growing need for data analysis techniques to extract valuable insights from complex biological data, as will be discussed in Section 6.

#### 4.2. *In vivo* SERS bioimaging

Noninvasive imaging methods like positron emission tomography/computerized tomography (PET/CT) and magnetic resonance imaging (MRI) are commonly used for clinical staging, to determine the extent of the disease in cancer patients. However, these techniques are susceptible to errors from potential artifacts, and techniques like PET can undesirably damage nearby tissue because of the use of high-energy radiation. In this context, SERS requires the application of a comparatively milder irradiation source,<sup>150</sup> has lower interference with tissue autofluorescence when using NIR SERS tags, and opens the door to multiplexed *in vivo* bioimaging.<sup>151</sup> In one example, Nie and co-workers showed the implementation of SERS imaging in a clinically practical setup, for the precise indication of tumor margins using a handheld pen (Fig. 9A).<sup>152</sup> The “Spectro Pen” incorporates a diode laser with 785 nm irradiation, in a compact head unit that acts as the light source and collection probe, connected *via* an optical fiber to a spectrometer for recording fluorescence and Raman signals. The collection of Stokes-shifted light is facilitated by the attenuation of Rayleigh scattered light using a dichroic mirror and long-pass filter, as well as by minimization of the silica signals from the fiber *via* physical filtering in the excitation and emission pathways.

More recently, tumor margin identification has been demonstrated for breast,<sup>153</sup> ovarian,<sup>151,154</sup> and brain<sup>155</sup> cancer xenograft models. The high imaging resolution provided by SERS is especially useful for identifying micrometastases or microtumors, which are microscopic collections of cancer cells that are often missed by standard imaging tests.<sup>153</sup> In the work of Wen and colleagues, SERS tags based on AuNSts were coated with the RaR 4-NTP, encapsulated in silica, functionalized with PEG-silane, and intravenously delivered into mice bearing 4T1 breast cancer tumors.<sup>156</sup> SERS imaging specifically indicated the tumor boundaries pre- and intra-operatively (Fig. 9D and E). Following resection of the primary tumor, SERS imaging of the surgical bed led to identification of multiple residual tumor foci and satellite microtumors (Fig. 9F). This work showed that SERS can be useful for ensuring complete removal of cancer cells, following image-guided resection.

Whereas tags built from NPs with LSPR in the first NIR biological window ( $\sim 700\text{--}950 \text{ nm}$ ) are the most common ones, scattering is further diminished at longer wavelengths, and

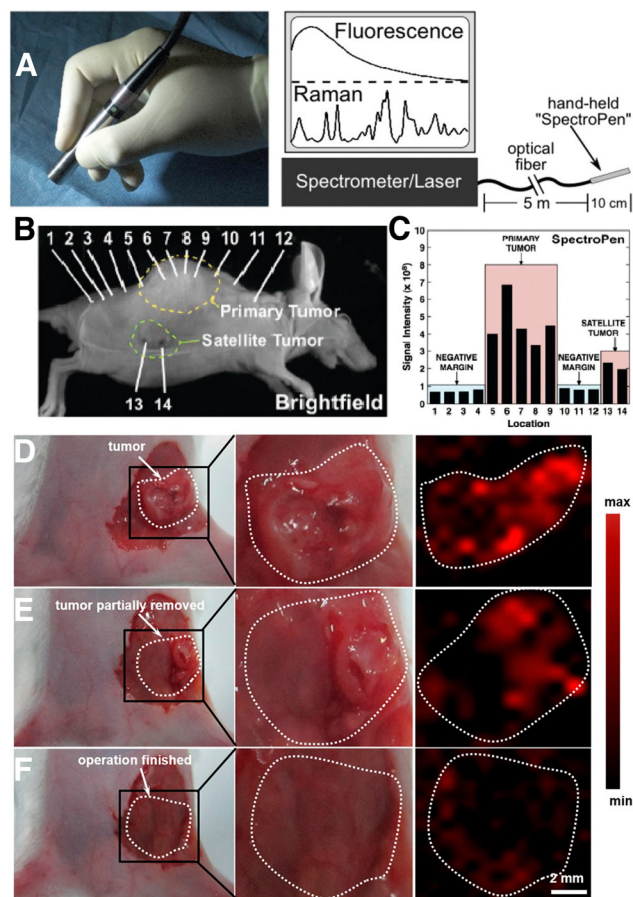


**Fig. 9** (A) Photograph (*left*) of a Raman imaging pen (“SpectroPen”) and schematic showing the measurement configuration. (B) Brightfield image of a mouse xenograft model with a 4T1 breast cancer tumor. (C) Results for mapping of primary and satellite tumor boundaries with the SpectroPen setup. [Adapted with permission from ref. 152 Copyright (2023) American Chemical Society] (D)–(F) digital photographs (*left* and *center*) and corresponding SERS images (*right*) of a 4T1 tumor-bearing mouse (D) prior to resection, (E) following partial removal of the tumor, and (F) after complete resection of the primary tumor. The bright regions in panel F correspond to residual microtumors. [Adapted with permission from ref. 156 Copyright (2021) American Chemical Society].

therefore recent works have explored the second biological window (NIR-II) at  $1000\text{--}1700 \text{ nm}$  for further extending the limits of resolution.<sup>154,157,158</sup> SERS tags targeting the NIR-II often include plasmonic cores comprising gold stars, cages, or nanorods with increased anisotropy (aspect ratio) or hollow structures.<sup>158</sup> In one example, Li and co-workers prepared porous AgAu nanocubes with LSPR in the NIR-II, capped with the dye IR 1061 as RaR and a polyethyleneimine/hyaluronic acid stabilizing shell. These tags were incubated in multicellular 4T1 breast cancer tumor spheroids for 12 h. Successful imaging of the spheroids following subcutaneous injection in animal models provided proof-of-concept demonstration that NIR-II tags could be used for imaging microtumors. In the same work, tags were also injected into the tail vein of solid tumor-bearing mice, which demonstrated nonspecific accumulation at the tumoral site due to the EPR effect. Overall, *in vivo*



imaging requires both high resolution and high throughput, with multimodal imaging offering an opportunity to improve both aspects, which we discuss in the following section.

### 4.3. Multimodal bioimaging

A wide variety of bioimaging modalities have been reported and implemented at different extent, each of them showing certain advantages and drawbacks. Therefore, numerous attempts have also been directed to the combination of technologies, which is usually known as multimodal bioimaging. Same as other modalities, SERS can also be combined with other techniques, in a way that advantage can be taken of mutual benefits for imaging biological models with high fidelity, resolution, and overall greater reliability and speed.<sup>159</sup> Multimodality can be achieved *e.g.*, by integrating plasmonic tags with magnetic components, for combined SERS, CT and MRI.<sup>160</sup> The combination of plasmonic and magnetic NPs can also be useful for therapeutic purposes, and gold coated-iron oxide NPs have demonstrated excellent performance in multimodal imaging, hyperthermia treatments, and drug delivery.<sup>161</sup> SERS can also be readily combined with photoacoustic imaging, which has been shown for anisotropic NPs like AuNRs and AuNSTs.<sup>151</sup> Yet another possibility is the correlation of SERS imaging with nanothermometry, which has been applied to monitor temperature at the nanoscale and to manage photo-thermal heating effects during SERS measurements.<sup>162,163</sup> As an example, rare earth-doped calcium fluoride NPs have been combined with AuNSTs and AuNRs to produce heater/thermometer nanotags that could be excited at the same wavelength within the biological transparency window, to heat and measure temperature within 3D tumor models.<sup>148,164</sup>

Overall, arguably the most common multimodal imaging combination for 3D cell models is dual SERS-fluorescence

imaging, whereby NPs are functionalized with both RaRs and fluorescent tags, to create dual-mode tags. Although we mainly focus on SERS-fluorescence multimodal imaging in this section, we direct the reader to other in-depth reviews on multimodal imaging, for extended information on other methods.<sup>159,165</sup>

In one example of SERS-fluorescence multimodal imaging, AuNRs coated with mesoporous silica shells were labelled with the RaR DTNB and the outer silica shell was doped with fluorescent Rhodamine B isothiocyanate (Fig. 10).<sup>166</sup> These dual tags were additionally conjugated with folic acid as a target ligand for HeLa cells. By tuning the wavelength of the excitation source, fluorescence (543 nm) and SERS signals (633 nm) could be generated separately. This type of dual nanotags has been employed to label MDA-MB-231 triple-negative breast cancer cells. In other examples, AuNPs were labelled with Malachite green isothiocyanate (MGITC) and tris(2,2'-bipyridyl)ruthenium(II) chloride hexahydrate (Ru(bpy)<sub>3</sub>) as RaRs, protected with an inner silica shell, and MGITC-modified fluorophores incorporated prior to an additional silica coating step. The intermediate coating with silica was intended to prevent the leaching of RaRs, as well as fluorescence quenching from the metal particle cores.<sup>167</sup> SERS tags can also be used in combination with fluorescently labelled polymer beads. For instance, AuNSTs adsorbed on fluorescent polystyrene beads can be tuned to improve the SERS signal, which has been used for multimodal imaging of Human lung epithelial cancer cells (adenocarcinomic human alveolar basal epithelial cells A549), MCF7 breast cancer cells, and murine J774 macrophages.<sup>168</sup>

The concept of multimodal imaging can be similarly applied to the visualization of scaffolds, as well as 3D models. Polymers, for example, can incorporate either dyes or SERS-labelled NPs, for combined use of both imaging techniques on a single

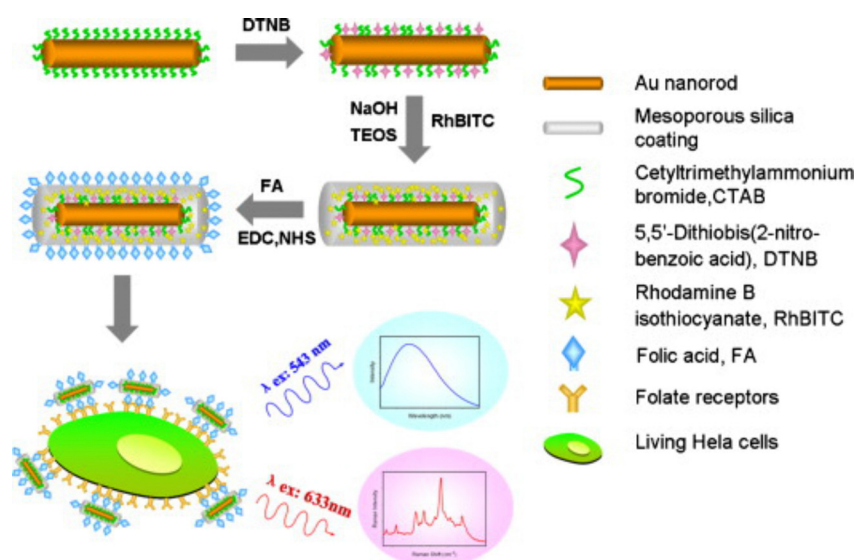


**Fig. 10** Schematic view of the fabrication of SERS-fluorescence nanotags for targeting cancer cells, using mesoporous silica-coated AuNRs. Three main steps were followed for the fabrication of the tag. First, the surface of AuNRs is labeled with DTNB as RaR. Then, an outer shell of mesoporous silica doped with Rhodamine B isothiocyanate is coated on the labelled AuNRs for fluorescence imaging. Finally, folic acid is conjugated on the surface of the particles as targeting ligand. [Adapted from ref. 166 with permission from Elsevier].



material. Strozyk *et al.* proposed the use of electrohydrodynamic co-jetting to prepare poly(lactic-co-glycolic acid) (PLGA) compartmentalized fibers, with dual fluorescence and SERS activity.<sup>169</sup> One of the polymer inks contained nanostars labelled with 4-BPT and a green dye, whereas the other was labelled with nanostars carrying 2-NAT and a blue dye. The absorption and emission profiles of the fluorescent dyes were selected to be far away from the excitation wavelength of the plasmonic cores in the SERS tags. 3D SERS and confocal fluorescence imaging were used to study the distribution of all labels inside the matrix, clearly demonstrating the compartmentalization of the fibers. In another work by the same authors, human dermal fibroblasts (HDF) were labelled with AuNSts and AuNRs functionalized with 1-NAT, 2-NAT, and 4-MBT, to prove the multiplexing ability of the technique toward imaging cell populations grown inside a scaffold (Fig. 11A and B).<sup>170</sup> When comparing the stability of the SERS tags with respect to the embedded dyes, under UV irradiation, photobleaching of the dyes was clearly observed whereas the SERS tags were not altered (Fig. 11C and D). The SERS signal intensity remained stable up to 4 days of incubation *in vitro*, but

was reduced after 8 days. When incorporated into the scaffolds, it was possible to image SERS-labelled HDFs up to 25 days *in vitro*, with a homogeneous distribution, also in the z-direction (100  $\mu\text{m}$ ). It is worth noting that complex data analysis, such as multiple linear regression analysis or true component analysis, are required for data postprocessing. The authors demonstrated that SERS imaging offers advantages for repetitive sample measurements with stable signals, an important aspect when monitoring cell models over prolonged periods.

SERS and fluorescence multimodal imaging also offers the possibility to perform *in vivo* deep tissue imaging. Among various options, NIR fluorescence-SERS tags are ideal candidates due to their high contrast and deeper detection ability, related to lower absorption and scattering of NIR light by biological tissue. The combination of both imaging techniques is particularly useful because fluorescence imaging can provide fast and wide-area detection to identify the target spot, whereas SERS offers high specificity and contrast at the nanotag location. For example, the distribution and excretion of intravenously injected AuNRs in deep tissues of live mice has been

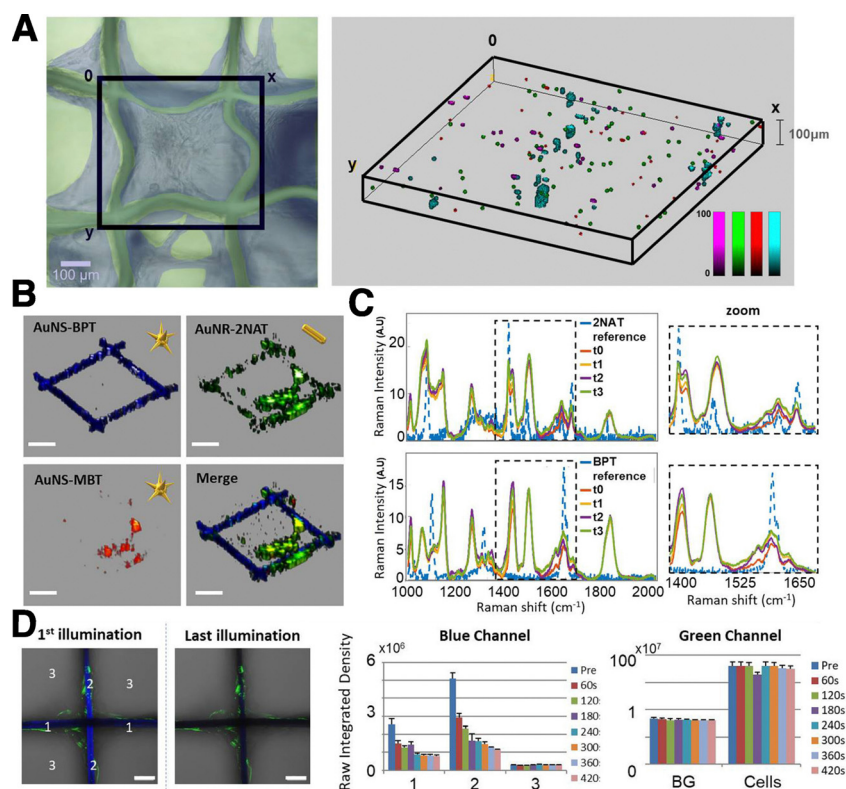


**Fig. 11** Comparison of SERS and fluorescence stability in multimodal scaffolds. (A) 3D SERS mapping of HDF cells after 25 DIV as viewed in bright field microscopy (left) and 3D SERS imaging (right). AuNSts labelled with 1-NAT (magenta), 2-NAT (green) and 4-MBT (red). Cells containing the three tags are shown in cyan. (B) Individual and merged 3D reconstructions of four different layers from different z-stack measurements. AuNSts labelled with 4-bisphenylthiol (4-BPT) (scaffold) appear in blue, AuNRs labelled with 2-NAT (HDF) are shown in green, and AuNSt labelled with 4-MBT (HDF) are shown in red (scale bars = 200  $\mu\text{m}$ ). (C) Photobleaching test using cell-internalized AuNRs labelled with 2-NAT and AuNSts labelled with BPT inside PLGA scaffolds. The area was repeatedly illuminated  $4\times$  for 1 h, with a 785 nm laser. For fluorescence imaging, a different area was irradiated  $7\times$  for 60 s, using a 405 nm laser. Images show the first and last illumination SERS maps, as well as the corresponding average spectra. Scale bars: 50  $\mu\text{m}$  (D) fluorescence imaging bleaching tests. Left images show the blue and green channels overlaid with the corresponding optical images for the first and last illuminations. Scale bars: 50  $\mu\text{m}$ . The bar graphs show the evolution of the fluorescence intensity for both fluorophores. [Adapted with permission from ref. 170 Copyright (2022) American Chemical Society].



reported to assess their toxicity and potential application.<sup>171</sup> Nanorods were coated with thiolated PEG and diethylthiatri-carbocyanine, both as fluorescent dye and RaR. The LSPR of AuNRs was tuned to avoid overlap with the fluorescence emission band of the RaR-dye, thereby preventing quenching. When the rods were subcutaneously injected to a mouse, real-time imaging was carried out by monitoring fluorescence, and SERS spectra were then recorded from the fluorescent site. When intravenously administered, AuNRs accumulated mostly in the liver of the mouse and partly in the tail. The intensity of the fluorescence signal was weaker than the one detected subcutaneously due to the location of the liver in the mouse body. However, the SERS spectra still had a high contrast in deep tissues and could be differentiated from the background. Sentinel lymph node mapping, as well as *in vivo* tumor targeting, were also explored following the same strategy, with bright fluorescent and SERS signals being obtained after 2 min and 24 h, respectively. Histological analysis revealed that a high amount of intravenously injected NPs did not induce any tissue/organ/nerve toxicity to mice. Along with multimodal imaging, these types of tags can be also employed for photodynamic therapy (PDT). As an example, silica-coated AuNRs were doped with protoporphyrin IX as a photosensitizer, to have them accumulate in the tumor site and ultimately combine multimodal imaging with PDT.<sup>172</sup> In short, SERS can be complemented with multiple techniques to investigate biological settings, fluorescence having been the most exploited modality so far.

#### 4.4. “Deep” SERS bioimaging techniques

Although we have seen significant developments based on traditional SERS setups, conventional measurement configurations are still limited by the penetration depth of light, which is only tens of mm at its best, even in the biological transparency window. For standard SERS measurements, optical clearing agents can be used to increase light penetration by reducing refractive index changes throughout the tissue (*i.e.*, *via* dehydration).<sup>173</sup> However, these techniques can be destructive to the sample, and are therefore primarily used for *ex vivo* analyses. Surface-enhanced resonance Raman spectroscopy (SERRS), a method pioneered by Stacy and Van Duyne for the analysis of tissues, is capable of accessing signal intensities that are orders of magnitude higher than those for standard SERS.<sup>174</sup> In SERRS, a laser line with a frequency closely matching an electronic excitation in the RaR is used to amplify the Raman scattering signal (Fig. 12A). The RaRs used for SERRS are usually dyes, selected to absorb light at wavelengths matching standard continuous-wave laser lines (532, 633, 785, 808 nm, *etc.*).<sup>174</sup> A number of studies have validated SERRS for 3D bioimaging,<sup>175,176</sup> as well as for sensing pH, oligonucleotides, thrombin, and other biologically relevant molecules.<sup>177–180</sup> Although SERRS gives comparable sensitivities to fluorescence-based approaches,<sup>181</sup> it can also provide information regarding the local microenvironment, while avoiding challenges related to photobleaching and the need for specific biological labels. Despite these benefits, SERRS tags must contain a chromophore

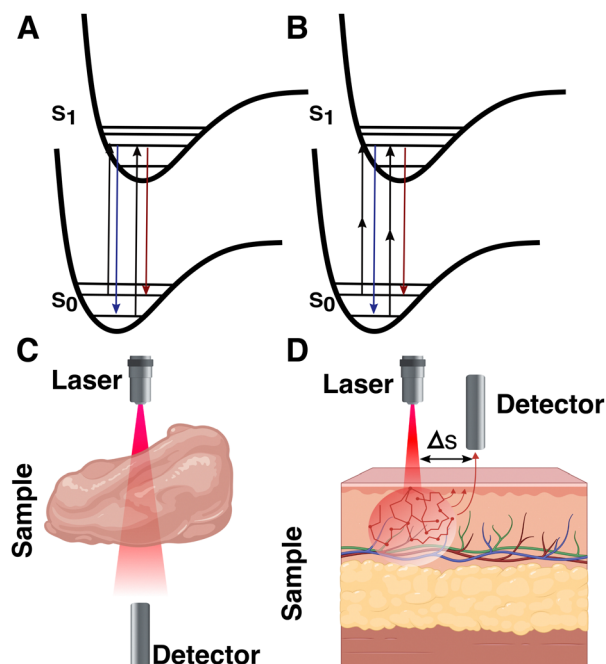


Fig. 12 Jablonski diagrams of (A) surface-enhanced resonance Raman spectroscopy (SERRS) and (B) surface-enhanced hyper-Raman scattering (SEHRS). Schematics showing the measurement configuration for (C) transmission Raman spectroscopy (TRS) and (D) basic spatially offset Raman spectroscopy (SORS).

at the illumination wavelength (preferably in the NIR) and provide a configurational response to the desired analytes or environmental changes, which is challenging.<sup>182</sup> This barrier may inhibit *in vivo* applications of SERRS. For instance, pH-sensitive SERRS tags have been reported to exhibit narrower sensitivity ranges ( $\sim 2\text{--}4$  pH units), compared to standard RaRs (reaching  $\sim 6$  or more pH units, required for pH sensing in organelles characterized by pH  $\sim 4\text{--}8$ ).<sup>183–186</sup> Surface-enhanced hyper-Raman scattering (SEHRS) in part offers a solution by performing the electronic excitation *via* a non-linear two-photon illumination process (at tunable wavelength), enabling resonance Raman for a wider breadth of RaRs (Fig. 12B). However, SEHRS requires a pulsed laser, whereas SERRS can be performed with more standard setups.<sup>187</sup>

There are many relevant cases where spectroscopic measurements should be made at depths beyond a few mm, *e.g.*, for deep-seated “phantom” and intracranial tumors.<sup>40</sup> Such extreme systems generally require alternative measurement setups whereby the configuration or position of the laser and/or detector are modified. Various “deep Raman imaging” techniques have been developed for this purpose, including transmission Raman spectroscopy (TRS), and (surface-enhanced) spatially offset Raman spectroscopy ((SE)SORS). Both TRS and SORS/SESORS improve the signal of scattered photons coming from deeper within a target material, by changing the spatial configuration of the source and detector. For the former, the detector is placed opposite the source. The latter method is more general, with the detector separated from the tag laser by certain distance ( $\Delta s$ ) and/or at a different angle (Fig. 12C and D).<sup>131,188</sup>



Early demonstrations by Matousek's team showed that the spectra corresponding to SERS tags embedded 50 mm deep in porcine muscle tissue could be detected with TRS *ex vivo*.<sup>131,189,190</sup> More recently, Zhang *et al.* applied TRS for 3D deep-seated tumor sensing *in vivo*, in nude mice.<sup>132</sup> While these works provide substantial and impressive improvement in 3D bioimaging/sensing compared to standard SERS, measurement in transmission requires the probe light to traverse completely through the sample. Therefore, this setup is not compatible with certain sample configurations or materials of widths greater than tens of mm, thereby limiting the *in vivo* applicability of the technique to (mainly) certain physical configurations in live mouse (or even smaller) models.

Compared to TRS, SESORS offers a more general solution for samples that are incompatible with transmission measurements.<sup>191</sup> The implementation of SESORS alone enables imaging in up to ~6 mm deep tissue<sup>192</sup> and ~3–5 mm of bone, for detecting RaRs<sup>193</sup> and biomolecules,<sup>194,195</sup> respectively. In one example, Moody *et al.* showed that SESORS (with 1 mm offset) could be applied to detect melatonin, epinephrine, and serotonin (distinguished using principal component analysis; PCA) in a synthetic brain model, through a 2 mm thick cat skull (Fig. 13A and B).<sup>194</sup> However, the limit of detection was only 100  $\mu\text{M}$ , a couple orders of magnitude higher than physiologically relevant concentrations. Later, Vo-Dinh and co-workers demonstrated SESORS detection of glioblastoma (but not 3D bioimaging) through a 5 mm monkey skull, which is comparable to human skulls with average bone thicknesses of 3–14 mm.<sup>195</sup> The sensing and imaging

depth accessible by SESORS can be further extended through combination with SERS, which is often referred to as SESORRS. This technique was applied to probing multicellular tumor spheroid breast cancer models, at depths up to 15 mm, and in porcine muscle tissues at 25 mm.<sup>196</sup>

For bioimaging through bone, Nicolson and co-workers carried out a notable study showing that SESORRS facilitates 3D bioimaging of mouse brains *in vivo* in live mice (Fig. 13C–E).<sup>197</sup> The SESORRS maps showed good agreement with MRI imaging of the tumor model (Fig. 13D and E). Measurement depth can be further maximized by combining resonance Raman with other imaging techniques, *e.g.*, in the work of Neuschmelting *et al.*, where image-guided brain tumor resection was achieved by combining SERS with multispectral optoacoustic tomography (MSOT).<sup>176</sup> Overall, these alternative SERS setups continue to push the limits of 3D spectroscopic analysis in tissue sections and *in vivo* environments. While an intensive account of alternative SERS techniques is beyond the scope of this review, we encourage those readers interested in learning about these methods to other comprehensive reviews on SERS,<sup>182,198</sup> TRS/SESORS,<sup>188,199</sup> and SEHRs.<sup>187</sup>

## 5. SERS biosensing in 3D

SERS is a powerful technique for interrogating cancer micro-environments, through the monitoring of biomarkers (such as growth factors, nucleotides, receptors, *etc.*), cell viability, or

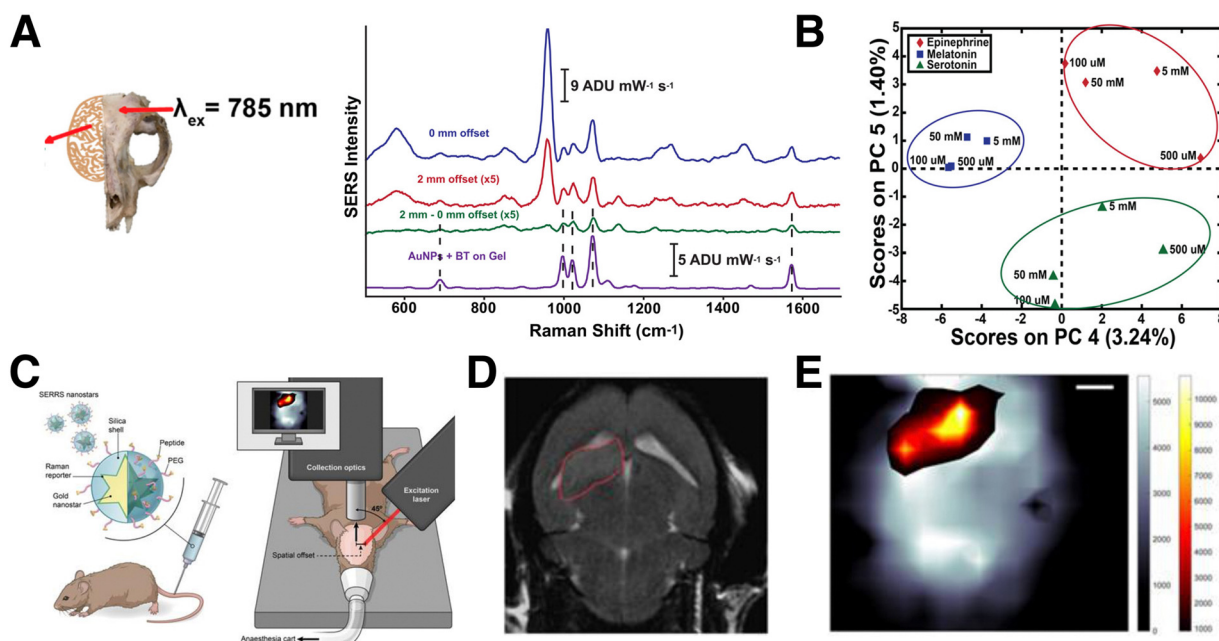


**Fig. 13** (A) Spectra obtained from a polymer brain model, through a cat skull (*inset*), without the addition of NPs or serotonin analyte (*blue*), after the addition of 100  $\mu\text{M}$  serotonin and NP tags with 0 offset (*pink*), after the addition of 100  $\mu\text{M}$  serotonin and NP tags with 1 mm offset (*green*), and of 100  $\mu\text{M}$  serotonin drop-cast on NP tags outside the mouse skull model on plain gel (*purple*). [Adapted with permission from ref. 194 Copyright (2017) American Chemical Society]. (B) Schematic view of a setup for SESORRS live mouse brain imaging. (C) 2D axial T2-weighted MRI measured 4 weeks following injection of fibroblasts in the region outlined in red, and (D) the corresponding SERS map, showing the overlay of the SERS tag signal (orange/yellow) and that corresponding to skull/bone (grayscale). [Adapted from ref. 197 with permissions from Ivyspring International Publisher]





local pH, among other possibilities, and at different levels of complexity, from serum samples and 3D cell cultures through 3D constructs.<sup>200</sup> The evaluation of both the tumor microenvironment and cancer-related cellular markers enables precise characterization of the tumor, which may yield diagnostic information and inform therapeutic strategies, because the overexpression of certain biomarkers is characteristic of disease evolution.<sup>201,202</sup> Additionally, SERS can also be used for combined theranostic studies.<sup>84,136,139,203–205</sup>

### 5.1. Sensing cancer-related biomarkers

Uncontrolled cell proliferation is mediated by many different signaling pathways, giving rise to a wide variety of valuable biomarkers, which can be more accurately studied in a 3D environment. For instance, biomarkers related to communication phenomena between tumor cells and the tumor microenvironment are often lacking in 2D models, but present in 3D.<sup>206</sup> Qian *et al.* studied the production of several biomarkers in 3D cultures by SERS. As an example, the interactions between tumoral and endothelial cells can induce angiogenesis, in turn promoting tumor growth and metastasis.<sup>207,208</sup> The production of the angiogenic cytokine vascular endothelial growth factor (VEGF) was monitored through the design of a multifunctional microfluidic platform combining the 3D cell culture unit with a SERS detection unit (Fig. 14). In the first unit, they co-cultured MCF-7 and human umbilical vein endothelial cells in a 3D collagen matrix (Fig. 14A). After a few days, culture medium was guided inside the SERS detection unit and the secretion of VEGF could be determined with a detection limit of  $100 \text{ pg mL}^{-1}$  (Fig. 14B). The applied SERS tags were composed of AuNRs functionalized with DTNB and an outer Ag layer for improved SERS enhancement (Au@DTNB@AgNRs), as well as aptamers for the selective detection of VEGF. The use of a SERS microfluidic chip was validated for

*in situ* interrogation of the tumor cell-endothelial cell interaction. Apart from angiogenesis inducers, adenosine also plays an important role in the development of tumors and metastases. García-Astrain *et al.* described the design of a scaffold for 3D cell culture and adenosine detection (down to  $10 \text{ } \mu\text{M}$ ), using 3D printed AuNR-containing scaffolds (see Section 3.3). Moreover, the scaffolds were shown to be fully biocompatible for HeLa cells.<sup>71</sup>

Surface receptors are commonly upregulated in tumoral cells to promote growth and ensure survival.<sup>209</sup> In fact, any abnormality in surface receptor regulation allows cells to escape apoptosis, thus playing key roles in many tumoral processes (proliferation, invasiveness, chemoresistance, *etc.*), and being appealing targets for therapy development and cancer tissue classification.<sup>210</sup> The cancer biomarker HER2 is upregulated in most breast cancers. Samanta *et al.* studied the expression of this receptor by cancer cells in mice bearing xenografts generated from SKBR-3 cells.<sup>211</sup> SERS tags were prepared by conjugating AuNPs coated with lipoic acid-containing amine acetylated tricarboyanines, which performed as RaRs, to two HER2-recognition motifs: anti-HER2 monoclonal antibody and single-chain fragment variable anti-HER2 antibody. The authors injected the NPs (tail-vein injection) into mice and obtained the SERS spectra of the tumor site through the skin, under NIR laser irradiation. The signal from the tricarboyanines on the tag was recorded only at the tumor site and no signal was detected at other anatomical locations, which indicates that SERS can specifically detect HER2 positive tumors *in vivo*.

Similar to multiplex bioimaging, whereby multiple RaRs are used, multiple biomarkers can be actively targeted *via* rational design of SERS tags. This approach can be beneficial for increasing diagnostic accuracy *in vivo*. For example, Dinish *et al.* reported the detection of three different cancer-related

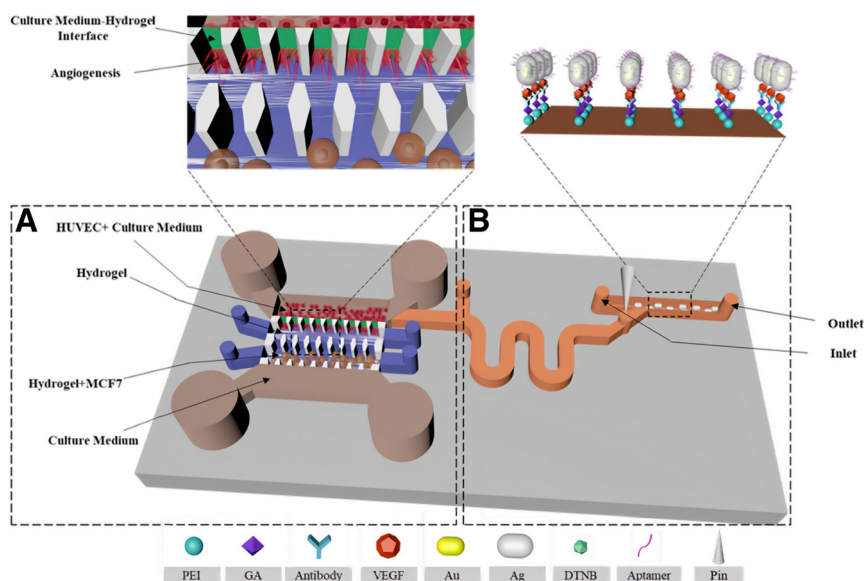
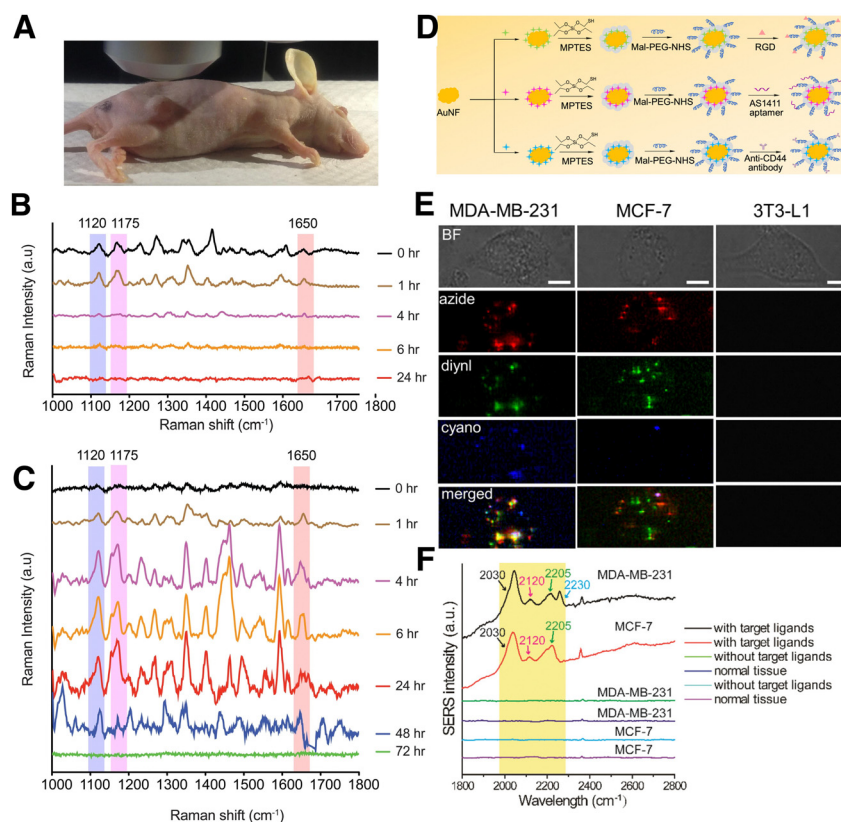


Fig. 14 Schematic illustration of a microfluidic chip for tumor cell culture (A) and SERS sensing (B). [Adapted with permission from ref. 208 Copyright (2019) American Chemical Society]



receptors (EGFR, CD44, and TGF $\beta$ RII) in a subcutaneous MDA-MB-231 breast cancer xenograft mouse model (Fig. 15A).<sup>212</sup> The authors used AuNPs bearing three different NIR-active RaRs, cyanine 5 (Cy5), MGITC, and rhodamine 6G (Rh6G), and three different antibodies against EGFR, a cell surface receptor for epidermal growth factor family members, CD44, a cell surface adhesion molecule related to tumor growth and metastasis, and TGF receptor II, which binds anti-proliferative TGF $\beta$  and is down-regulated during breast carcinogenesis. The efficacy of active targeting was supported by comparing SERS spectra in control mice that were injected with non-antibody conjugated tags to those injected with antibody-conjugated tags. In the former, the disappearance of the RaR spectra was observed after 1 h due to elimination of the NPs from the models (Fig. 15B). In the latter, the peaks related to the RaRs were still observed after 48 h due to selective binding of the antibodies with their receptors, causing a delay in elimination (observed after 72 h; Fig. 15C).

Beyond antibodies, aptamers serve as low-cost alternatives for multiplex detection that retain the affinity and specificity of antibodies while displaying lower immunogenicity and longer tissue penetration (like small molecules). In recent examples by Tang's group, breast cancer diagnostic capabilities of aptamer-functionalized SERS tags were explored. MCF7 cells are known to overexpress nucleolin (a Bcl-2 mRNA binding protein involved in apoptosis regulation) and Mucin 1 (a transmembrane glycoprotein that plays a role in metastasis). Bioorthogonal nanotags were functionalized by attaching dithiolane and diynl RaRs to AuNRs then adding lipoic acid labelled oligonucleotide aptamers A1411 and MUC1 for targeting nucleolin and Mucin 1, respectively.<sup>138,139</sup> Both tag types showed significantly higher uptake in MCF7 cells compared to mouse fibroblasts *in vitro*. Following tail vein injection in MCF7 tumor-bearing mice, the particles accumulated in the liver, spleen, and tumor, but showed no pathological effects on the main organs, therefore exhibiting good biocompatibility and capacity



**Fig. 15** *In vivo* detection of cancer-related biomarkers in a xenograft tumor: (A) Setup for experiments in tumor bearing mice. (B) Control SERS spectra from tumor site showing the peaks at 1120, 1175, and 1650  $\text{cm}^{-1}$  right after injection of non-antibody bearing SERS tags and quick clearance from the mouse body due to non-specific bonding. (C) Representative SERS spectra from the tumor site, showing the peaks at 1120, 1175, and 1650  $\text{cm}^{-1}$  from the antibody conjugated SERS tags bound to TGF $\beta$ RII, CD44, and EGFR biomarkers, respectively. Multiplex SERS spectra were recorded up to 48 hours, followed by tag clearance from the mouse body after  $\sim$ 72 hours. [Adapted from ref. 212 with permissions from Springer Nature]. (D) Scheme describing the fabrication of bioorthogonal SERS tags: gold nanoflowers (AuNF) are functionalized with (3-mercaptopropyl)triethoxysilane (MPTES), which is then coupled to either a targeting peptide (RGD), aptamer (AS1411), or antibody (anti-CD44), *via* coupling with a maleimide and NHS ester functionalized polyethylene glycol (Mal-PEG-NHS; Mn = 5 kDa). (E) Multiplex SERS image of breast cancer (MDA-MB-231 and MCF7) and healthy cells (3T3-L1) after incubation with the SERS tags. The maps reveal the presence of azide (2120  $\text{cm}^{-1}$ , red), vinyl (2205  $\text{cm}^{-1}$ , green), and cyano (2230  $\text{cm}^{-1}$ , blue) groups, corresponding to the aptamer, RGD peptide, and antibody coated tags, respectively. (F) SERS spectra obtained from MDA-MB-231 and MCF-7 tumor-bearing mice after intravenous delivery of SERS tags, highlighting the intensities of the cyano, azide, and vinyl peaks. [Adapted with permission from ref. 138,139 Copyright (2019) American Chemical Society].



for specific identification of MCF7 cells. Later, the same group used a combination of Arg-Gly-Asp (RGD) peptide, aptamers (A1411), and anti-CD44 coatings for their binding to breast cancer MCF7 and MDA-MB-231 cells both *in vitro* and *in vivo* (Fig. 15D). MDA-MB-231 overexpress CD44 compared to MCF7, therefore, there was comparatively high localization of the tags functionalized with anti-CD44 in MDA-MB-231 2D cell cultures and tumors (Fig. 15E and F). These results ultimately point towards possibilities for aptamer- and antibody-functionalized SERS tags for distinguishing between different cancers.

## 5.2. Sensing in cancer therapeutics

One of the most appealing applications of 3D cell models comprises testing of antitumoral drugs, which is not only expected to reduce the use of animal models, but also to be more efficient as a high-throughput platform. The incorporation of SERS may serve to monitor spectral changes of cellular metabolites (*i.e.*, cholesterol, trypsin, guanine), as shown by Altunbek and colleagues, to test the chemotherapeutic response of HeLa cell spheroids to doxorubicin and paclitaxel.<sup>213</sup> Similarly, Kapara *et al.* analyzed the drug response of estrogenic receptor alpha (ER $\alpha$ )-positive breast cancer spheroids.<sup>119</sup> MCF7 breast cancer cells were targeted with SERS tags coated with 1,2-bis(4-pyridyl) ethylene (BPE) and anti-ER $\alpha$ , and the effect of the drug Fulvestrant on tag uptake was evaluated. Further than just tracking drug efficacy, 3D scaffolds containing AuNRs were employed by Plou *et al.* to uncover the diffusion profile of SERS-active drugs. More specifically, they studied the diffusion rate of methylene blue (MB, a photosensitizer used in photodynamic therapy of cancer) through a 3D MCF-7 culture,<sup>72</sup> and correlated drug diffusion with cell death in a custom cell culture device (Fig. 16A). This study involved the design of a chip where the plasmonic scaffold was printed from a plasmonic bioink of label-free AuNRs and gelatin-alginate, ultimately yielding a suitable spatiotemporal resolution for mapping the diffusion of MB through MCF-7 cell-laden Matrigel (Fig. 16B and C).

It is also worth mentioning that, when working with complex biological samples, the task of pinpointing distinctive SERS fingerprints for specific biomolecules is challenging, primarily due to the coexistence of numerous components within the same sample. Consequently, establishing a direct correlation between vibrational peaks and the presence of specific metabolites becomes a difficult task. In this context, incorporating techniques such as multivariate analysis and artificial intelligence, machine learning in particular, has become an interesting solution. Such techniques range from fundamental principal component analysis (PCA), which simplifies the dimensionality of SERS spectra to reveal data variations, to more advanced machine learning methods like deep learning, which extract pertinent information and utilize it for data classification.<sup>214</sup>

## 5.3. Theranostics

Although the primary focus of this review is on 3D SERS bioimaging and biosensing, we find it valuable to briefly

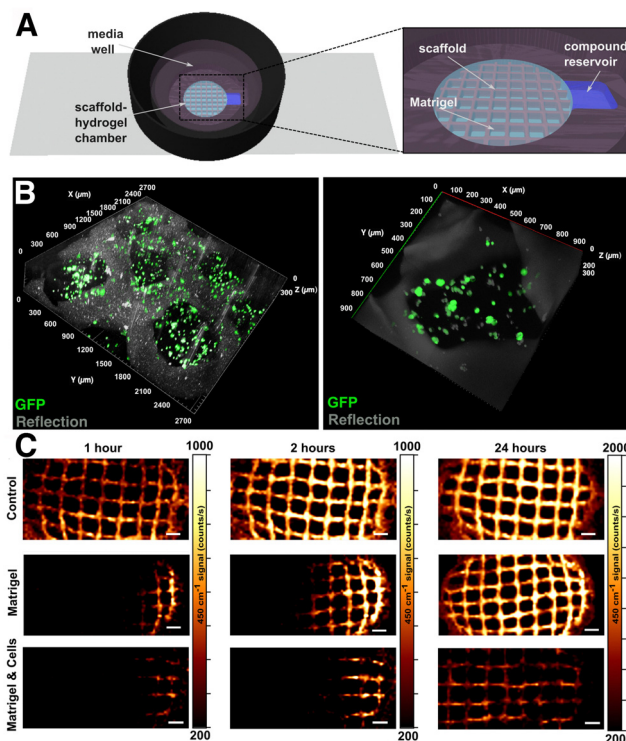


Fig. 16 (A) Setup integrating nanocomposite scaffolds within a tumor cell environment and a reservoir for drug delivery. (B) Confocal 3D reconstruction of MCF-7 cells embedded in Matrigel within the supporting scaffold. (C) MB diffusion patterns along the X-axis in the scaffolds, scaffolds embedded in Matrigel, and Matrigel loaded with cells. [Adapted with permissions from ref. 72 Copyright (2021) American Chemical Society].

discuss some recent developments in “theranostics”, that is, the simultaneous application of SERS tags for diagnostic and therapeutic purposes, a widely explored area often pursued in tandem with SERS biosensing/imaging. As mentioned in the beginning of Section 3, thermoplasmonic heating may be one of the main challenges when performing SERS measurements on biological materials. Even though it is usually desirable to minimize thermoplasmonic heating, the same effect can be exploited for therapeutic purposes. For example, Zeng *et al.* explored thermal ablation of breast cancer (MCF7) cells *in vitro* and *in vivo* in tumor-bearing mice.<sup>215</sup> They used SERS to track the accumulation of the designed tags – Ag<sub>core</sub>@Au<sub>shell</sub> nano-stars capped with the dye 3,3'-diethylthiatricarbocyanine iodide (RaR) – in the tumor. In this design, the gold shell assisted in shielding the Ag core, thereby improving biocompatibility. With 80% light-to-heat conversion at 808 nm irradiation, photothermal heating under 140 mW irradiation for 10 s reduced cell viability down to ~5%.

Active targeting ligands can also be used for specific binding to upregulated proteins and more efficient delivery of SERS tags to tumor sites *in vivo*, followed by combined detection, bioimaging, and PTT.<sup>138</sup> In one example, Pal and colleagues designed multimodal SERS tags based on AuNRs selectively binding to folate receptor 1 (FOLR1) in breast cancer cells. *In vivo* and *in vitro* studies showed preferential uptake by MDA-MB-468



cells due to their overexpression of FOLR1, compared to MCF-7 and MDA-MB-231 cells. Following a mild photothermal treatment at  $3 \text{ W cm}^{-2}$  for 5 min, specific reduction in size of MDA-MB-468 tumors was achieved. Photothermal treatment may also require the combined use with other techniques, to ensure full tumor removal. Recently, Wen *et al.* demonstrated 100% tumor removal with silica-coated AuNSts tags, containing PNTP and a PEG stabilizing coating. Even though the light-to-heat conversion was lower than in the previous examples (44.7% at 808 nm), image-guided resection (see Section 4.3) proved highly effective toward removing the primary tumor and subsequently residual microtumors by thermoplasmonic heating.

Thermonanoplasmonic SERS tags can also carry chemotherapeutics, for combined photothermal therapy (PTT)-chemotherapy. Yin *et al.* developed silica-coated AuNSts tags, subsequently coated with gold sphere satellite structures, then finally functionalized with RGD and doxorubicin.<sup>216</sup> This configuration led to high doxorubicin loading efficiency into HeLa cells, as well as >85% light-to-heat conversion. *In vivo* SERS measurements showed that nanocarriers functionalized with 4-MBA were efficiently retained at the injection site within tumor-bearing mice, for at least 2 h. Upon triggering localized heating by irradiation with NIR light, doxorubicin was selectively released. Ultimately, thermoplasmonic heating yielded five-fold higher nuclear loading of doxorubicin, compared to the negative control, and tumor size was shown to decrease irreversibly after an irradiation treatment of just 5 min.

#### 5.4. pH sensing

Aside from biomarkers, pH is a key parameter of cell micro-environments because cellular activity is influenced or followed by pH changes. As a general example, intracellular pH (pHi) homeostasis is disrupted when cells undergo apoptosis.<sup>217</sup> It is well known that cancer cells exhibit different pHi and extracellular pH (pHe) profiles compared to normal cells, due to the Warburg effect, which describes how cancer cells undergo aerobic glycolysis at higher rates than healthy cells (Fig. 17). Detection of pHi provides useful information regarding early cancer cell development, viability, invasion behaviors, and nanomaterial endocytic pathways, whereas pHe monitoring enables complementary information on viability, invasion, and proliferation, and has practical utility for identifying tumor boundaries (3D SERS image-guided tumor excision).<sup>218</sup>

Ideally, a pH sensor should provide biologically appropriate precision and sensing range, achieve high/targeted intracellular delivery (in the case of pHi), and be effective and easy to implement in realistic 3D models. Thus far, various strategies for monitoring pH in 2D and 3D have been developed, including those that incorporate electrochemical measurements/nanoprobes, pH-sensitive fluorophores, metal oxide thin films, conductive polymers, and plasmonic nanomaterials.<sup>219–222</sup> As emphasized in the earlier sections, compared to other approaches, SERS pH tags are attractive because they are exceptionally photostable, sensitive with a broad sensing range, minimally invasive, highly multiplexable, and capable of providing additional chemical information about the surrounding

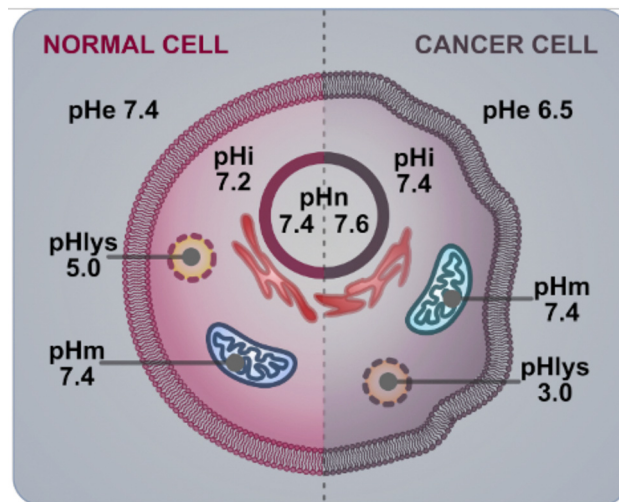
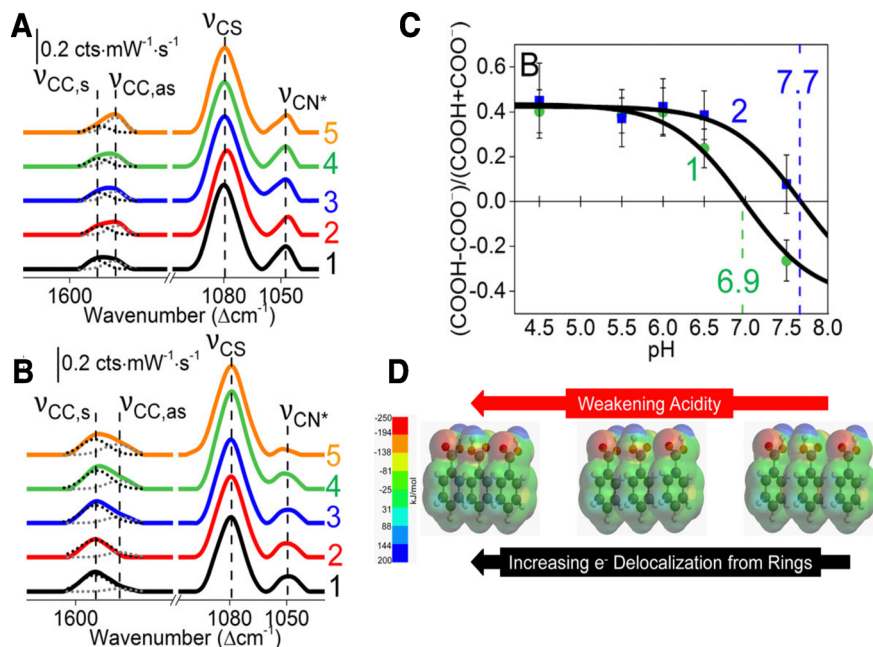


Fig. 17 Diagram comparing the pH profile of a healthy and a cancerous cell.

environment. As pH sensors, plasmonic NPs coated with pH-responsive ligands are capable of high sensitivity (down to  $\sim 0.1$  pH units) and may cover tunable sensing ranges (2–12 pH), depending on the chosen nanomaterial and ligand, for evaluation of either pHi or pHe. Two of the most common pH-responsive RaRs include 4-MPy and 4-MBA. In most cases, pH is determined using a the “ratiometric approach,” whereby the SERS spectra are recorded in buffer solutions with different pH values, then, the change in intensity or integrated peak area of one or more (summed) select pH-sensitive peaks is evaluated. Finally, the ratio between the pH-sensitive peaks and a non-pH sensitive base peak is evaluated, and the values are fit to a calibration curve following the Henderson–Hasselbalch equation. The curve is then used to calculate an unknown pH value from SERS spectra measured from the sample.

The SERS spectra of pH-sensitive molecules, as with other RaRs, depends on their concentration and orientation, which is influenced by their packing density and the particle’s composition and crystal structure. For pH sensitive RaRs, the packing density can also influence the effective  $pK_a$ , which in turn modulates the sensing range and the overall calibration curve for the sensor. In the work by Phan and Haes,  $\text{Ag@Au@SiO}_2$  NPs functionalized with 4-MBA were prepared with different incubation times.<sup>223</sup> These authors monitored SERS peak shifts and changes in intensity while pH was raised from 4.5 to 7.5 in 1-unit increments (Fig. 18A and B). Ratiometric comparison of the intensity of pH sensitive peaks (indicated by black dashed lines Fig. 18A and B) to the base peak (the C–S stretching,  $\nu_{CS}$  at  $1080 \text{ cm}^{-1}$ ) showed that longer incubation times (18 h) gave a  $\sim 1$  unit higher estimated  $pK_a$  value ( $pK_a = 7.7$ ) compared to shorter incubation times ( $pK_a = 6.9$  at 30 min) (Fig. 18C). This difference was attributed to the increased ligand density and  $\pi$ – $\pi$  stacking interactions. Increased  $\pi$ – $\pi$  stacking resulted in a decrease of electron density in the rings and an increase of electron density at the carboxylic acid group, thereby increasing the bond strength of the COO–H group and reducing the acidity





**Fig. 18** (A) and (B): SERS spectra of Ag@Au@SiO<sub>2</sub> incubated with 4-MBA for (A) 30 min and (B) 18 h at different pH values: (1) 4.5, (2) 5.5, (3) 6.0, (4) 6.5, and (5) 7.5. (C) Comparison of ratiometrically prepared calibration curves for tags incubated for 30 min (green text, pK<sub>a</sub> 6.9) and 18 h (blue text, pK<sub>a</sub> 7.7). (D) Energy density simulations of 4-MBA ligands with increasing packing density (from left to right), showing that higher density is associated with stronger acidity. [Adapted with permission from ref. 223 Copyright (2018) American Chemical Society].

(Fig. 18D).<sup>223</sup> Although this study was carried out using a 2D plasmonic substrate, the result is ultimately important for the accurate and effective implementation of pH sensors in 3D systems, and is important to consider when measuring pHi or pHe, which will be discussed using concrete examples in the following sections.

**5.4.1. Intracellular pH sensing.** Works on pHi SERS sensing have mainly focused on achieving sufficient subcellular resolution and pH sensitivity, as well as targeting the appropriate intracellular regions/organelles, *i.e.*, in the mitochondria, endosomes, cytoplasm, *etc.* Achieving these goals constitutes a major challenge and, as a result, many studies focus on pHi sensing in 2D cell cultures, rather than in 3D. Nonetheless, the results from these systems provide insights that might be applied to 3D systems in the future. For example, the work of Zhang *et al.* developed pH SERS tags based on AuNSt@4-MBA and explored their intracellular delivery in 2D cultures of MCF7 breast cancer cells. To optimize cell uptake of the tags, the surface charge imparted by the RaR was considered as a relevant parameter. Tags functionalized with 4-MBA are stable in aqueous solution due to their overall negative charge at neutral pH, where the carboxylic acid group is predominantly deprotonated (pK<sub>a</sub> ~ 5–7 when bound to a surface/NP; bulk pK<sub>a</sub> ~ 4) (Fig. 19A).<sup>213,224</sup> Because the cell membrane bears a negative charge, intracellular delivery could only be achieved through additional coating with a positively charged polymer, on top of the negatively-charged RaR. The polymer coating was shown to significantly improve uptake, from negligible quantities up to 30–60% after only a few hours of incubation (as evaluated with ICP-MS; Fig. 19B).<sup>183,225</sup>

The uptake of tags into lysosomes could be precisely tracked using 3D SERS mapping (Fig. 19C). Although 4-MBA has a narrower pH sensing range compared to other pH sensitive RaRs like 4-MPy, the polymer coating on AuNSt@4-MBA was shown to not only improve the stability of the tag (against oxidative reshaping of the AuNSt core), but also to improve its sensing range from 5–6 to ~4.5–7.5 (Fig. 19D). This difference was attributed to an effect the polymer layer on the diffusion of protons to the bound 4-MBA molecules, as well as on the 4-MBA orientation with respect to the substrate surface. Kneipp and co-workers demonstrated a further improved sensing range of pH 2–8 with 4-MBA-capped tags, by using SEHRS (see Section 4.4).<sup>187,226</sup>

Compared to 4-MBA, the other common pH sensitive RaR, 4-MPy, is primarily in its deprotonated neutral form at pH higher than ~3, and therefore lacks sufficient Coulombic repulsion to remain stable in aqueous suspension or biological media. Zheng and co-workers demonstrated that the colloidal stability of 4-MPy-coated gold nanospheres could be improved by conjugation to different biomolecules.<sup>227</sup> In their work, it was shown that subsequent functionalization with the protein bovine serum albumin (BSA) could stabilize the structures within a range of pH 5.5 to 9.0, compared to non-BSA functionalized tags, which exhibited aggregation. These AuNP@4-MBA@BSA tags were shown to maintain colloidal stability, even in high ionic strength solutions. Similar to the results of the 4-MBA study, the coated tags exhibited more reliable and reproducible pH sensing, as well as high cell uptake (CaSki; human cervical epidermoid carcinoma), compared to non-functionalized tags. In a later work from the same group,



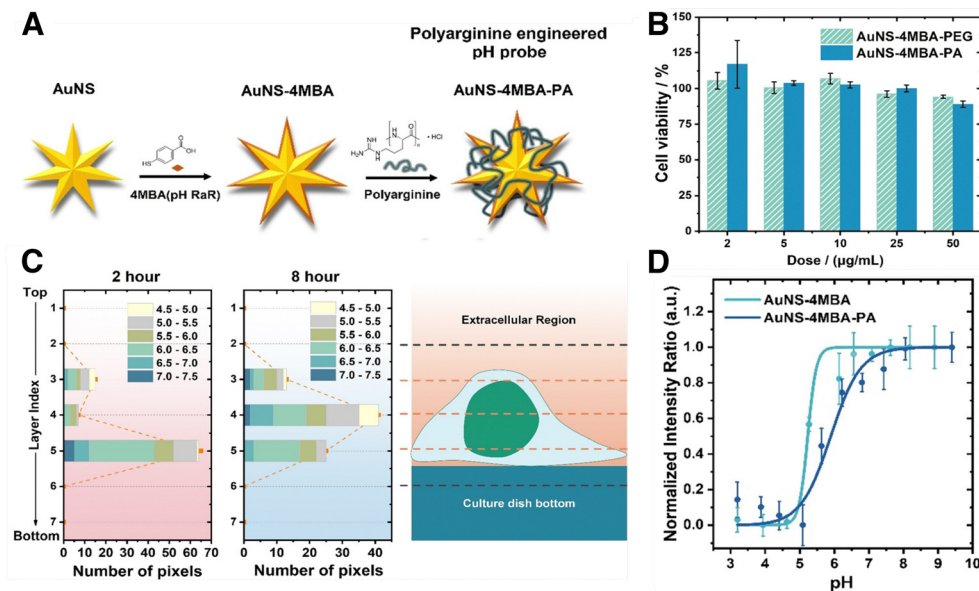


Fig. 19 (A) Scheme illustrating the fabrication of pH SERS tags from AuNSs capped with pH-sensitive 4-MBA and PA. (B) Uptake of tags capped with PEG and positively charged poly-L-arginine by MCF7 breast cancer cells, evaluated with inductively coupled plasma mass spectrometry. (C) Analysis of particle distribution and sensed pH, in an individual cancer cell over time. (D) Comparison of pH sensing calibration curve from tags with and without PA stabilizing coating. [Adapted with permission from ref. 183 Copyright (2020) American Chemical Society].

subsequent functionalization with a cell penetrating peptide (transactivator of transcription, TAT) led to further enhanced cell uptake after 2 h incubation, as evaluated by comparing the SERS intensities of the  $1093\text{ cm}^{-1}$  characteristic peak of 4-MPy.<sup>140</sup> Notably, the cells exhibited a uniform distribution of the tags throughout the cytoplasm, whereas without the TAT peptide coating the tags have difficulty escaping lysosomes, ultimately limiting detailed pH studies in the subcellular regime. Other important considerations for pH<sub>i</sub> measurements include the potential errors that may arise due to interference from the background, as demonstrated by Capocefalo and colleagues.<sup>228</sup> Their study showed that pH estimation could be inaccurate by several tenths of a pH unit depending on overlap of cell-related signals and the pH-sensitive peaks. Thus, high-accuracy measurements from the ratiometric approach should consider the background SERS spectra or apply environments that exactly recapitulate the conditions of the sample. For pH<sub>i</sub> sensing, where there are unavoidable and non-uniform background signals from proteins and lipids, implementing either of these two approaches would be time-consuming and challenging. In addition, beyond absolute and integrated peak intensities, some works also suggest that monitoring peak shifts can further enhance the pH-sensitivity.<sup>229</sup>

**5.4.2. Extracellular pH sensing.** The implementation of pHe SERS monitoring has been tested to evaluate cell viability under different conditions. In 2D cultures, substrates composed of AuNPs coated with 4-MPy could discriminate between normal and cancer cells *via* pHe measurements, which was applied to monitor cancer cell behavior upon addition of a tumor suppressor: transforming growth factor- $\beta$  (TGF- $\beta$ ).<sup>230,231</sup> Initially, the pHe at regions containing the cells gave acidic readings, but various phenomena could be observed after

spiking the 2D cell cultures with TGF- $\beta$ , including cell deformation and acidification of non-cell-containing regions. This result was rationalized as being due to the release of protons built-up in the extracellular region to the surrounding environment, as membrane disruption and apoptosis occurred. Ultimately, this work showed that pHe SERS monitoring could assist in probing the efficacy of therapeutics for different cancer cell lines.

So far, pHe sensing in 3D configurations has been demonstrated in microencapsulated cells, organoids, and tissues. In the work of Zhou, pHe sensing was performed for cells contained in semipermeable alginate membranes (Fig. 20A and B).<sup>225</sup> One challenge for the real-world implementation of encapsulated cell therapies is the death of cells within such membranes. SERS sensing could be used to map acidification at the capsule periphery (Fig. 20C and D). In Fig. 20E, it can be observed that capsules containing dead cells had a significantly lower pH than those with live ones, which was supported by metabolic characterization (Fig. 20F). Skinner *et al.* developed pHe tags with high SERS signals *via* the assembly of dense gold nanosphere coatings on polystyrene microspheres, further functionalized with 4-MBA.<sup>232</sup> These tags were applied to test the accumulation of metabolic acids in patient-derived airway organoid models, relevant for studies of cystic fibrosis. Notably, pH differences as low as 0.1 units could be identified, demonstrating that the 3D configuration contributes to the production of acidic metabolites that, in turn, provide appropriate conditioning of the microenvironment. Overall, the implementation of this design for other types of organoids could have far reaching impact toward the development of disease models incorporating SERS sensors. In a recent study by Choudhury and colleagues on *ex vivo* ovine lung models, accuracies of



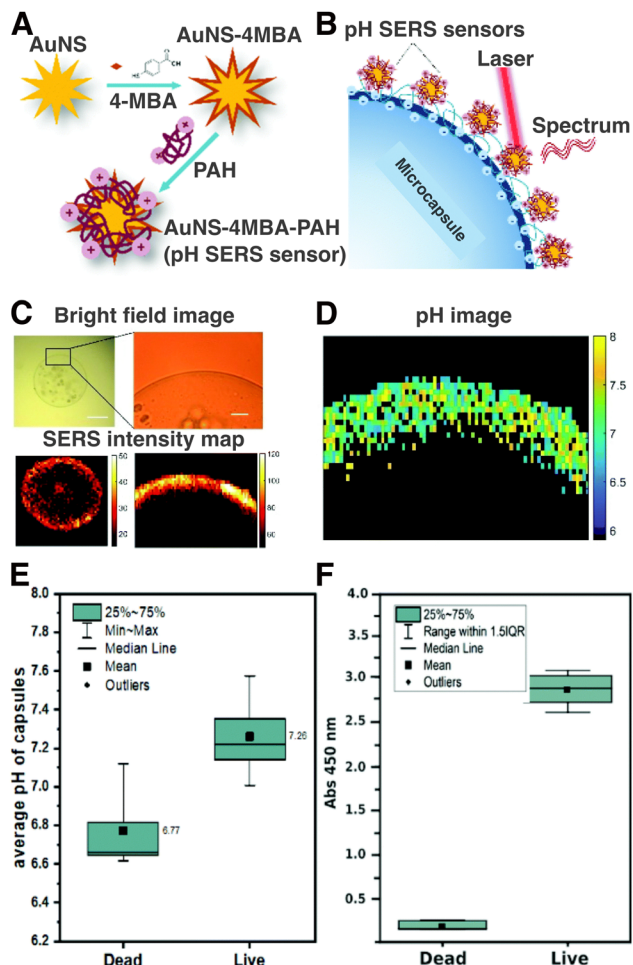


Fig. 20 (A) Schematic fabrication process of pH-sensitive SERS tags capped with pH-responsive 4-MBA and stabilizing PAH. (B) Configuration of pH sensors on alginate microcapsules containing Murine C2C12 myoblasts. (C) Brightfield image (top) of microencapsulated cells and the corresponding SERS map (bottom). (D) Map of pH distribution at the microcapsules derived from SERS mapping. (E) and (F): graphs comparing the (E) pH and (F) metabolic activity of dead and live microencapsulated cells 24 h after labelling. [Adapted from ref. 225 with permission from the Royal Society of Chemistry].

$\pm 0.07$  pH units could be achieved using an endoscopic optrode functionalized with gold nanoshells@4-MBA for alveolar pH sensing. Despite the advances in sensitivity of pH-responsive SERS nanotags, there are still very few examples of pHe sensors for *ex vivo* and *in vivo* applications.

Finally, similar limitations to the ratiometric approach also apply for pHe sensing, creating opportunities for the exploitation of more advanced data analysis methods like PCA and machine learning. While PCA alone does not solve the issue of variable contributions from the background, Williams *et al.* showed that pH changes can be captured with higher precision using PCA, with  $\sim 70\%$  lower error for each pH value compared to the ratiometric approach.<sup>233</sup> For machine learning, a key study by Vikesland's group validated several multivariate regression models for pH prediction with 4-MPy-functionalized stacked gold nanodisk arrays, demonstrating successful

pH determination across five different media (not utilized for model training).<sup>234</sup> Overall, while machine learning analysis has progressed significantly for SERS sensing of biomolecules,<sup>235,236</sup> the implementation of such techniques for both pHe and pHi in biological systems is still in its early stages, and can be a key element paving the way for more successful demonstrations of SERS pH sensing in complex 3D environments.

### 5.5. Practical considerations for SERS clinical application

SERS holds great promise for various clinical applications. However, practical implementation of this technology in clinical settings presents its own set of challenges. On one hand, for routine diagnostic implementation of SERS *in vivo*, it is imperative to navigate through various regulatory frameworks and conduct comprehensive safety evaluations regarding nanomaterials administration. Such considerations depend on national regulations and, therefore, require a region-specific approach. The challenges are many, for example: nanomaterials/nanomedicines lack a unified classification criterion; analytical procedures differ from one nanomaterial to another; current pre-clinical biodistribution and toxicological studies fail to mimic the real complexity of human body; *etc.*<sup>237</sup> There are few examples of clinical implementation of nanomaterials, mainly encompassing polymeric micelles, liposomes, and lipid nanoparticles, whereas few examples of metallic nanomaterials have made it to the market and the clinic.<sup>238</sup> In the case of AuNPs, several systems have reached various stages of clinical trials, but none has been clinically approved to date.<sup>239</sup> Ultimately, despite these challenges, some strategies may be pursued to achieve clinical approval. For instance, the use of simple nanotag compositions (few components) can speed-up the approval process, and also benefit production scalability. Targeting high risk/mortal diseases with a need for novel therapeutics, *i.e.*, cancer, should also increase the probability of clinical approval. Overall, it is important that any clinical risks (accumulation of gold in the body and other side effects) are outweighed by the benefit of using AuNP systems, meaning that they should result in a higher therapeutic efficacy.

On the other hand, the ease of implementation of SERS measurements in the clinic also requires consideration. In many of the SERS platforms highlighted so far, the end goal is to develop devices compatible with *in vitro* cell cultures and *ex vivo* screening of patient samples (*i.e.*, patient-derived 3D models, biopsies, microfluidic sensing, *etc.*). In this regard, easy-to-use, and simple instrumentation that can be readily integrated into existing medical and diagnostic workflows are needed. Conventional Raman spectrometers have an optical configuration in which lasers can be applied *via* flexible optical fibers to excite the sample and collect the scattered light. Therefore, Raman spectrometers are easily customizable. Actually, various designs for handheld Raman instruments compatible with clinical settings have been developed for *in situ* measurements, such as the SpectroPen described in Section 4.2, many of them being commercially available.<sup>240,241</sup> Moreover, available spectral analysis software can assist in



interpretation of the spectra for molecular identification, to facilitate clinical use. However, one of the primary challenges here is the cost of instrument components: laser light source(s), high-performance optical fibers, *etc.* An additional constraint arises from the limited penetration depth of the excitation laser into body tissues, which restricts its application to superficial or readily accessible tumors. A significant stride forward occurred in 2015, with the release of an endoscopic probe designed for SERS imaging.<sup>242</sup> Nevertheless, it is crucial to address these obstacles, to fully harness the potential benefits of SERS in medical diagnostics and treatment monitoring.

## 6. Summary and outlook

In this review, we highlight the importance of constructing 3D biomimetic models, and give an overview of the fabrication techniques and common geometries applied in these systems. General design rules and strategies for incorporating SERS tags within 3D systems are discussed. It is noted that SERS tags should be biocompatible, stable in biologically relevant conditions, and strongly interact with the target system/analyte. Then, the latest developments in 3D SERS bioimaging and sensing are summarized. Some important considerations regarding SERS bioimaging include minimizing or making additional considerations to address the scattering background, using appropriate data processing tools, and multimodal bioimaging for enhancing contrast. Regarding biosensing in 3D systems, SERS substrates can be used to analyze secreted biomolecules/metabolites from 3D models, which has been explored using microfluidic platforms.<sup>208,235,243,244</sup> SERS sensors can also be directly incorporated into the 3D model, and this configuration has been applied, both for differentiating between cell types and for tracking certain parameters of the microenvironment, including pH.

Based on the research progress so far, we can identify various areas that require further exploration, namely: (i) fully leveraging the capabilities of SERS for chemical and biomolecule identification in 3D, (ii) improving multiplexing possibilities, (iii) refining signal processing tools, (iv) addressing limitations towards clinical and practical implementation of SERS, and (v) expanding 3D SERS bioimaging and biosensing beyond 3D cancer models. While SERS has been successfully implemented for the quantitative detection in 2D of a multitude of analytes, including therapeutics,<sup>245</sup> neurotransmitters,<sup>246</sup> metabolites/proteins,<sup>247–249</sup> reactive oxygen species,<sup>250,251</sup> DNA,<sup>252</sup> pathogens,<sup>253</sup> and more,<sup>200</sup> still very few works take full advantage of the rich chemical information that SERS can provide in 3D systems. The implementation of label-free SERS in 3D models that recapitulate real biological environments or with *ex/in vivo* models, could provide key insights at the molecular level for early diagnosis and disease monitoring and/or for the development of novel therapies.

One of the advantages of SERS imaging is the possibility to customize SERS tags to target specific tumor microenvironments, which play a key role in the resulting efficacy of diagnostic and therapeutic approaches. SERS tags can be

conjugated with a series of antibodies, aptamers, or biomolecules, which can be tailored to achieve a unique cocktail for simultaneous targeting of different cell types. Taking into account the diverse characteristics of different cancer types, SERS precision and sensitivity could be improved. Responsive and dynamic SERS probes could also be useful to adapt to cancer progression and recognize temporal changes within the tumor microenvironment. Responsiveness to changes in the composition of the cell membrane or external parameters, such as pH or temperature, could pave the way toward smart SERS tags that can dynamically adapt to the tumor microenvironment. By exploring the tailored design of SERS tags for specific tumor microenvironments, we have the potential to elevate the precision, sensitivity, and clinical applicability of SERS technologies for effective cancer therapies.

In terms of multimodal bioimaging, there are many examples combining SERS with fluorescence-based imaging, however, other imaging modes could also be coupled with SERS, which have been comparatively under-explored in 3D models, including magnetic, acoustic, and thermometric-based imaging. We finally provided some examples where complex SERS signals require processing *via* advanced data analysis techniques and machine learning. We propose that the continued development of user-friendly analytical tools is imperative, especially for the advancement of quantitative biosensing in complex environments. Although the specific focus of this review was mainly geared toward cancer applications, we note that there are still very few examples of 3D SERS bioimaging and biosensing for other diseases, such as for the study of Alzheimer's,<sup>254</sup> Parkinson's,<sup>255</sup> cystic fibrosis,<sup>232</sup> immune disorders,<sup>256</sup> *etc.* Additionally, the emerging implementation of chiral plasmonic NPs, either functionalized into different substrate/host materials or in colloidal suspension, may add enantiomeric specificity for SERS sensing, which is another crucial aspect of drug development.<sup>257</sup>

## Table of acronyms

Acronym	Definition
AgNP	Silver nanoparticle
AgNR	Silver nanorod
AuNP	Gold nanoparticle
AuNR	Gold nanorod
AuNSt	Gold nanostar
ATP	4-aminothiophenol
BSA	Bovine serum albumin
4-BPT	4-bisphenylthiol
BT	Benzenethiol
CT	Computerized tomography
Cy5	Cyanine 5
DTNB	5,5'-dithiobis(2-nitrobenzoic acid)
dECM	Decellularized extracellular matrix
ECM	Extracellular matrix
EGFR	Epidermal growth factor receptor
EpCAM	Epithelial cell adhesion molecule





HeLa	Henrietta Lacks cervical cancer cell line
HER2	Human epidermal growth factor receptor 2
HDF	Human dermal fibroblasts
ICP-MS	Ion coupled plasma- mass spectroscopy
J774	Macrophage cell line
LSPR	Localized surface plasmon resonance
4-MBA	4-mercaptobenzoic acid
4-MBT	4-methylbenzenethiol
MCF7	Michigan Cancer Foundation 7 cell line
MDA	M. D. Anderson epithelial human breast cancer cell line
MDA-MB-231	Epithelial human breast cancer cell line
MGITC	Malachite green isothiocyanate
4-MPy	4-mercaptopyridine
MRI	Magnetic resonance imaging
MSOT	Multispectral optoacoustic tomography
4-MSTP	4-(methylsulfanyl)thiophenol
1-NAT	1-naphthalenethiol
2-NAT	2-naphthalenethiol
NBT	nitrobenzenethiol
NIR	Near-infrared
NP	Nanoparticle
2-NPT	2-naphthalenethiol
4-NTP	4-nitrothiophenol
PA	Poly-L-arginine hydrochloride
PAH	Poly(allylamine hydrochloride)
PALM	Photo-activated localization microscopy
4-ATP	4-aminothiophenol
PCA	Principal component analysis
PC3	Human prostatic carcinoma cell line
PDT	Photodynamic therapy
PDX	Patient-derived xenograft
PEG	Poly(ethylene glycol)
PET	Positron emission tomography
PI-DETA	Poly(isoprene)-diethylenetriamine
PI- <i>b</i> -PEG	Poly(isoprene)- <i>block</i> -poly(ethylene glycol)
PLGA	Poly(lactic- <i>co</i> -glycolic acid)
PMA	Dodecylamine-modified polyisobutylene- <i>alt</i> -maleic polymer
4-NTP	4-nitrothiophenol
PVA	poly(vinyl alcohol)
PVP	Polyvinylpyrrolidone
RaR	Raman reporter molecule
Rh6G	Rhodamine 6G
Ru(bpy) <sub>3</sub>	tris(2,2'-bipyridyl)ruthenium(II) chloride hexahydrate
SEM	Scanning electron microscopy
SEHRS	Surface-enhanced hyper Raman spectroscopy
(SE)SORS	(Surface-enhanced) spatial-offset Raman spectroscopy
SERS	Surface-enhanced Raman spectroscopy
SERRS	Surface-enhanced resonance Raman spectroscopy
STED	Stimulated emission depletion microscopy
STORM	Stochastic optical reconstruction microscopy
4T1	Human breast cancer cell line

TEM	Transmission electron microscopy
TERS	Tip-enhanced Raman spectroscopy
TGF-β	Transforming growth factor-β
TRS	Transmission Raman spectroscopy
UV	Ultraviolet
U87-MG	Human glioblastoma cell line
VEGF	Vascular endothelial growth factor
2D	Two-dimensional
3D	Three-dimensional

## Conflicts of interest

There are no conflicts to declare.

## Acknowledgements

Financial support was provided by the European Research Council (ERC-AdG-2017 #787510) and by the European Comision (EUSMI, Grant Number 731019). C.G.A. thanks the Spanish State Research Agency for a Juan de la Cierva Incorporación Fellowship (IJC2019-040827-I). L.T.A. thanks the Spanish Ministry of Universities for a Formación de Profesorado Universitario Fellowship (FPU-05867). Fig. 1, 2, 5 and 10 were created using BioRender.com.

## References

- J. J. Hornberg, F. J. Bruggeman, H. V. Westerhoff and J. Lankelma, *BioSystems*, 2006, **83**, 81–90.
- H. Sung, J. Ferlay, R. L. Siegel, M. Laversanne, I. Soerjomataram, A. Jemal and F. Bray, *Ca-Cancer J. Clin.*, 2021, **71**, 209–249.
- C. Sawyers, *Nature*, 2004, **432**, 294–297.
- Q. Gao, G. Zhou, S. Lin, R. Paus and Z. Yue, *Exp. Dermatol.*, 2019, **28**, 413–418.
- L. Hutchinson and R. Kirk, *Nat. Rev. Clin. Oncol.*, 2011, **8**, 189–190.
- N. M. Anderson and M. C. Simon, *Curr. Biol.*, 2020, **30**, R921–R925.
- M. Timaner, O. Beyar-Katz and Y. Shaked, *Curr. Protoc. Cell Biol.*, 2016, **70**, 19.18.1–19.18.12.
- R. C. Dutta and A. K. Dutta, *Biotechnol. Adv.*, 2009, **27**, 334–339.
- S. R. Horman, C. Hogan, K. D. Reyes, F. Lo and C. Antczak, *Future Med. Chem.*, 2015, **7**, 513–525.
- K. Kingwell, *Nat. Rev. Drug Discovery*, 2017, **16**, 6–7.
- R. Edmondson, J. J. Broglie, A. F. Adcock and L. Yang, *Assay Drug Dev. Technol.*, 2014, **12**, 207–218.
- R. Augustine, S. N. Kalva, R. Ahmad, A. A. Zahid, S. Hasan, A. Nayeem, L. McClements and A. Hasan, *Transl. Oncol.*, 2021, **14**, 101015.
- E. C. Costa, A. F. Moreira, D. De Melo-Diogo, V. M. Gaspar, M. P. Carvalho and I. J. Correia, *Biotechnol. Adv.*, 2016, **34**, 1427–1441.



- 14 J. W. Lichtman and J.-A. Conchello, *Nat. Methods*, 2005, **2**, 910–919.
- 15 D. Davydova, A. de la Cadena, D. Akimov and B. Dietzek, *Laser Photonics Rev.*, 2016, **10**, 62–81.
- 16 J. Zhang, R. E. Campbell, A. Y. Ting and R. Y. Tsien, *Nat. Rev. Mol. Cell Biol.*, 2002, **3**, 906–918.
- 17 J. Choi, E. K. Lee, J. Choo, J. Yuh and J. W. Hong, *Biotechnol. J.*, 2015, **10**, 1682–1688.
- 18 A. R. Kherlopian, T. Song, Q. Duan, M. A. Neimark, M. J. Po, J. K. Gohagan and A. F. Laine, *BMC Syst. Biol.*, 2008, **2**, 74.
- 19 A. Downes and A. Elfick, *Sensors*, 2010, **10**, 1871–1889.
- 20 D. I. Ellis, D. P. Cowcher, L. Ashton, S. O'Hagan and R. Goodacre, *Analyst*, 2013, **138**, 3871–3884.
- 21 E. Brauchle and K. Schenke-Layland, *Biotechnol. J.*, 2013, **8**, 288–297.
- 22 M. Fleischmann, P. J. Hendra and A. J. McQuillan, *Chem. Phys. Lett.*, 1974, **26**, 163–166.
- 23 J. A. Creighton, *Vibrational Spectroscopy of Adsorbates*, Springer-Verlag, Berlin Heidelberg, New York, 1980, vol. 15, pp. 145–164.
- 24 F. W. King, R. P. Van Duyne and G. C. Schatz, *J. Chem. Phys.*, 1978, **69**, 4472–4481.
- 25 T. Itoh, M. Procházka, Z.-C. Dong, W. Ji, Y. S. Yamamoto, Y. Zhang and Y. Ozaki, *Chem. Rev.*, 2023, **123**, 1552–1634.
- 26 S. Schlücker, *Surface Enhanced Raman Spectroscopy: Analytical, Biophysical and Life Science Applications*, John Wiley & Sons, 2011.
- 27 S. M. Morton and L. Jensen, *J. Am. Chem. Soc.*, 2009, **131**, 4090–4098.
- 28 M. Procházka, *Surface-Enhanced Raman Spectroscopy*, Springer International Publishing, Cham, 2016.
- 29 S. Schlücker, *ChemPhysChem*, 2009, **10**, 1344–1354.
- 30 S. A. Maier, *Plasmonics: fundamentals and applications*, Springer, 2007, vol. 1.
- 31 D. K. Gramotnev and S. I. Bozhevolnyi, *Nat. Photonics*, 2010, **4**, 83–91.
- 32 M. Moskovits, *Rev. Mod. Phys.*, 1985, **57**, 783–826.
- 33 R. Alvarez-Puebla, L. M. Liz-Marzán and F. J. García de Abajo, *J. Phys. Chem. Lett.*, 2010, **1**, 2428–2434.
- 34 P. Nordlander, C. Oubre, E. Prodan, K. Li and M. I. Stockman, *Nano Lett.*, 2004, **4**, 899–903.
- 35 F. Hao, C. L. Nehl, J. H. Hafner and P. Nordlander, *Nano Lett.*, 2007, **7**, 729–732.
- 36 N. Valley, N. Greeneltch, R. P. Van Duyne and G. C. Schatz, *J. Phys. Chem. Lett.*, 2013, **4**, 2599–2604.
- 37 Y. Fang, N.-H. Seong and D. D. Dlott, *Science*, 2008, **321**, 388–392.
- 38 K. A. Willets and R. P. Van Duyne, *Annu. Rev. Phys. Chem.*, 2007, **58**, 267–297.
- 39 J. Langer, D. Jimenez de Aberasturi, J. Aizpurua, R. A. Alvarez-Puebla, B. Auguie, J. J. Baumberg, G. C. Bazan, S. E. J. Bell, A. Boisen, A. G. Brolo, J. Choo, D. Cialla-May, V. Deckert, L. Fabris, K. Faulds, F. J. García de Abajo, R. Goodacre, D. Graham, A. J. Haes, C. L. Haynes, C. Huck, T. Itoh, M. Käll, J. Kneipp, N. A. Kotov, H. Kuang, E. C. Le Ru, H. K. Lee, J.-F. Li, X. Y. Ling, S. A. Maier, T. Mayerhöfer, M. Moskovits, K. Murakoshi, J.-M. Nam, S. Nie, Y. Ozaki, I. Pastoriza-Santos, J. Perez-Juste, J. Popp, A. Pucci, S. Reich, B. Ren, G. C. Schatz, T. Shegai, S. Schlücker, L.-L. Tay, K. G. Thomas, Z.-Q. Tian, R. P. Van Duyne, T. Vo-Dinh, Y. Wang, K. A. Willets, C. Xu, H. Xu, Y. Xu, Y. S. Yamamoto, B. Zhao and L. M. Liz-Marzán, *ACS Nano*, 2020, **14**, 28–117.
- 40 P. G. Etchegoin and E. C. Le Ru, *Phys. Chem. Chem. Phys.*, 2008, **10**, 6079–6089.
- 41 J. Kneipp, *ACS Nano*, 2017, **11**, 1136–1141.
- 42 A. Kamińska, E. Witkowska, K. Winkler, I. Dziegielewska, J. L. Weyher and J. Waluk, *Biosens. Bioelectron.*, 2015, **66**, 461–467.
- 43 H. Kearns, R. Goodacre, L. E. Jamieson, D. Graham and K. Faulds, *Anal. Chem.*, 2017, **89**, 12666–12673.
- 44 Z. Cheng, R. Wang, Y. Xing, L. Zhao, J. Choo and F. Yu, *Analyst*, 2019, **144**, 6533–6540.
- 45 Y. Zhou, J. Liu, T. Zheng and Y. Tian, *Anal. Chem.*, 2020, **92**, 5910–5920.
- 46 S. S. Panikar, G. Ramírez-García, S. Sidhik, T. Lopez-Luke, C. Rodriguez-Gonzalez, I. H. Ciapara, P. S. Castillo, T. Camacho-Villegas and E. De La Rosa, *Anal. Chem.*, 2019, **91**, 2100–2111.
- 47 H.-Y. Wu and B. T. Cunningham, *Nanoscale*, 2014, **6**, 5162–5171.
- 48 G. A. Vinnacombe-Willson, *Surface Functionalization, Patterning, and in Situ Growth of Gold Nanoparticles*, University of California, Los Angeles, 2022.
- 49 K. Białkowska, P. Komorowski, M. Bryszewska and K. Miłowska, *Int. J. Mol. Sci.*, 2020, **21**, 6225.
- 50 A. Moscona and H. Moscona.
- 51 F. Pampaloni, E. G. Reynaud and E. H. K. Stelzer, *Nat. Rev. Mol. Cell Biol.*, 2007, **8**, 839–845.
- 52 J. W. Haycock, *3D cell culture: a review of current approaches and techniques*, Springer, 2011.
- 53 X. Cui, Y. Hartanto and H. Zhang, *J. R. Soc., Interface*, 2017, **14**, 20160877.
- 54 E. C. Costa, A. F. Moreira, D. De Melo-Diogo, V. M. Gaspar, M. P. Carvalho and I. J. Correia, *Biotechnol. Adv.*, 2016, **34**, 1427–1441.
- 55 S. F. Abu-Absi, J. R. Friend, L. K. Hansen and W.-S. Hu, *Exp. Cell Res.*, 2002, **274**, 56–67.
- 56 S. J. Han, S. Kwon and K. S. Kim, *Cancer Cell Int.*, 2021, **21**, 152.
- 57 D. Antoni, H. Burckel, E. Josset and G. Noel, *Int. J. Mol. Sci.*, 2015, **16**, 5517–5527.
- 58 M. W. Tibbitt and K. S. Anseth, *Biotechnol. Bioeng.*, 2009, **103**, 655–663.
- 59 M. C. Cushing and K. S. Anseth, *Science*, 2007, **316**, 1133–1134.
- 60 Y. C. Choi, J. S. Choi, B. S. Kim, J. D. Kim, H. I. Yoon and Y. W. Cho, *Tissue Eng., Part C*, 2012, **18**, 866–876.
- 61 L. T. Saldin, M. C. Cramer, S. S. Velankar, L. J. White and S. F. Badylak, *Acta Biomater.*, 2017, **49**, 1–15.
- 62 N. A. Peppas, J. Z. Hilt, A. Khademhosseini and R. Langer, *Adv. Mater.*, 2006, **18**, 1345–1360.



- 63 D. Seliktar, *Science*, 2012, **336**, 1124–1128.
- 64 J. Thiele, Y. Ma, S. M. C. Bruekers, S. Ma and W. T. S. Huck, *Adv. Mater.*, 2014, **26**, 125–148.
- 65 J. Lou and D. J. Mooney, *Nat. Rev. Chem.*, 2022, **6**, 726–744.
- 66 C. Vila-Parrondo, C. García-Astrain and L. M. Liz-Marzán, *Adv. Colloid Interface Sci.*, 2020, **283**, 102237.
- 67 D.-W. Cho, B. S. Kim, J. Jang, G. Gao, W. Han and N. K. Singh, *3D Bioprinting: Modeling In Vitro Tissues and Organs Using Tissue-Specific Bioinks*, Springer International Publishing, 2019.
- 68 S. Kyle, Z. M. Jessop, A. Al-Sabah and I. S. Whitaker, *Adv. Healthcare Mater.*, 2017, **6**, 1700264.
- 69 S. V. Murphy and A. Atala, *Nat. Biotechnol.*, 2014, **32**, 773–785.
- 70 J. Rosendahl, A. Svanström, M. Berglin, S. Petronis, Y. Bogestål, P. Stenlund, S. Standoft, A. Ståhlberg, G. Landberg, G. Chingacarrasco and J. Håkansson, *Bioengineering*, 2021, **8**, 97.
- 71 C. García-Astrain, E. Lenzi, D. Jimenez De Aberasturi, M. Henriksen-Lacey, M. R. Binelli and L. M. Liz-Marzán, *Adv. Funct. Mater.*, 2020, **30**, 2005407.
- 72 J. Plou, B. Molina-Martínez, C. García-Astrain, J. Langer, I. García, A. Ercilla, G. Perumal, A. Carracedo and L. M. Liz-Marzán, *Nano Lett.*, 2021, **21**, 8785–8793.
- 73 D. L. Hughes, A. Hughes, Z. Soonawalla, S. Mukherjee and E. O'Neill, *Cancers*, 2021, **13**, 2870.
- 74 C. Perleberg, A. Kind and A. Schnieke, *Dis. Models Mech.*, 2018, **11**, dmm030783.
- 75 Y. Liu, W. Wu, C. Cai, H. Zhang, H. Shen and Y. Han, *Signal Transduction Targeted Ther.*, 2023, **8**, 160.
- 76 L. G. Campana, M. Bullo, P. Di Barba, F. Dughiero, M. Forzan, M. E. Mognaschi, P. Sgarbossa, A. L. Tosi, A. Bernardis and E. Sieni, *Technol. Cancer Res. Treat.*, 2018, **17**, 1533033818789693.
- 77 J. Jung, *Toxicol. Res.*, 2014, **30**, 1–5.
- 78 L. Pompili, M. Porru, C. Caruso, A. Biroccio and C. Leonetti, *J. Exp. Clin. Cancer Res.*, 2016, **35**, 1–8.
- 79 J. J. Morton, G. Bird, Y. Refaeli and A. Jimeno, *Cancer Res.*, 2016, **76**, 6153–6158.
- 80 Z. Lei, X. Ren, S. Wang, X. Liang and Y. Tang, *OncoTargets Ther.*, 2016, 545–555.
- 81 K. Majumder, N. Arora, S. Modi, R. Chugh, A. Nomura, B. Giri, R. Dawra, S. Ramakrishnan, S. Banerjee and A. Saluja, *J. Gastrointest. Surg.*, 2016, **20**, 53–65.
- 82 J. Jin, K. Yoshimura, M. Sewastjanow-Silva, S. Song and J. A. Ajani, *Cancers*, 2023, **15**, 4352.
- 83 A. Khademhosseini and R. Langer, *Nat. Protoc.*, 2016, **11**, 1775–1781.
- 84 K. C. Bantz, A. F. Meyer, N. J. Wittenberg, H. Im, Ö. Kurtuluş, S. H. Lee, N. C. Lindquist, S.-H. Oh and C. L. Haynes, *Phys. Chem. Chem. Phys.*, 2011, **13**, 11551–11567.
- 85 T. Köker, N. Tang, C. Tian, W. Zhang, X. Wang, R. Martel and F. Pinaud, *Nat. Commun.*, 2018, **9**, 607.
- 86 S. Yu, Y. Yin, J. Chao, M. Shen and J. Liu, *Environ. Sci. Technol.*, 2014, **48**, 403–411.
- 87 J. Liu, K. G. Pennell and R. H. Hurt, *Environ. Sci. Technol.*, 2011, **45**, 7345–7353.
- 88 F. Wang, R. G. Widejko, Z. Yang, K. T. Nguyen, H. Chen, L. P. Fernando, K. A. Christensen and J. N. Anker, *Anal. Chem.*, 2012, **84**, 8013–8019.
- 89 R. Shukla, V. Bansal, M. Chaudhary, A. Basu, R. R. Bhonde and M. Sastry, *Langmuir*, 2005, **21**, 10644–10654.
- 90 X. Huang, S. Neretina and M. A. El-Sayed, *Adv. Mater.*, 2009, **21**, 4880–4910.
- 91 B. Andreiuk, F. Nicolson, L. M. Clark, S. R. Panikkanvalappil, M. Rashidian, S. Harmsen and M. F. Kircher, *Nanotheranostics*, 2022, **6**, 10–30.
- 92 J. Xie, Q. Zhang, J. Y. Lee and D. I. C. Wang, *ACS Nano*, 2008, **2**, 2473–2480.
- 93 S. E. Skrabalak, J. Chen, Y. Sun, X. Lu, L. Au, C. M. Copley and Y. Xia, *Acc. Chem. Res.*, 2008, **41**, 1587–1595.
- 94 X. Zhuo, D. Vila-Liarte, S. Wang, D. Jimenez de Aberasturi and L. M. Liz-Marzán, *Chem. Mater.*, 2023, **35**, 5689–5698.
- 95 G. Baffou, F. Cichos and R. Quidant, *Nat. Mater.*, 2020, **19**, 946–958.
- 96 R. Rodríguez-Oliveros and J. A. Sánchez-Gil, *Opt. Express*, 2012, **20**, 621–626.
- 97 G. Baffou and R. Quidant, *Laser Photonics Rev.*, 2013, **7**, 171–187.
- 98 E. Lenzi, M. Henriksen-Lacey, B. Molina, J. Langer, C. D. L. de Albuquerque, D. Jimenez de Aberasturi and L. M. Liz-Marzán, *ACS Sens.*, 2022, **7**, 1747–1756.
- 99 G. A. Vinnacombe-Willson, N. Chiang, L. Scarabelli, Y. Hu, L. K. Heidenreich, X. Li, Y. Gong, D. T. Inouye, T. S. Fisher, P. S. Weiss and S. J. Jonas, *ACS Cent. Sci.*, 2020, **6**, 2105–2116.
- 100 Y.-T. Yang, I.-L. Hsu, T.-Y. Cheng, W.-J. Wu, C.-W. Lee, T.-J. Li, C. I. Cheung, Y.-C. Chin, H.-C. Chen, Y.-C. Chiu, C.-C. Huang and M.-Y. Liao, *Anal. Chem.*, 2019, **91**, 8213–8220.
- 101 E. Lázaro-Ibáñez, F. N. Faruqu, A. F. Saleh, A. M. Silva, J. Tzu-Wen Wang, J. Rak, K. T. Al-Jamal and N. Dekker, *ACS Nano*, 2021, **15**, 3212–3227.
- 102 E. Lenzi, D. Jimenez de Aberasturi and L. M. Liz-Marzán, *ACS Sens.*, 2019, **4**, 1126–1137.
- 103 X.-S. Zheng, P. Hu, Y. Cui, C. Zong, J.-M. Feng, X. Wang and B. Ren, *Anal. Chem.*, 2014, **86**, 12250–12257.
- 104 A. S. D. S. Indrasekara, B. J. Paladini, D. J. Naczynski, V. Starovoytov, P. V. Moghe and L. Fabris, *Adv. Healthcare Mater.*, 2013, **2**, 1370–1376.
- 105 H. Wang, H. Zhang, L. Zhang, S. Zhao, Y. Chen, Y. Wan, Q. Zhang and L. Xia, *RSC Adv.*, 2021, **11**, 37443–37448.
- 106 S. Lee, H. Chon, J. Lee, J. Ko, B. H. Chung, D. W. Lim and J. Choo, *Biosens. Bioelectron.*, 2014, **51**, 238–243.
- 107 D. Jimenez de Aberasturi, M. Henriksen-Lacey, L. Litti, J. Langer and L. M. Liz-Marzán, *Adv. Funct. Mater.*, 2020, **30**, 1909655.
- 108 D. Jimenez de Aberasturi, A. B. Serrano-Montes, J. Langer, M. Henriksen-Lacey, W. J. Parak and L. M. Liz-Marzán, *Chem. Mater.*, 2016, **28**, 6779–6790.
- 109 M. Schumacher, D. Jimenez de Aberasturi, J.-P. Merkl, L. Scarabelli, E. Lenzi, M. Henriksen-Lacey, L. M. Liz-Marzán and H. Weller, *Adv. Opt. Mater.*, 2022, **10**, 2102635.



- 110 X. Zhuo, M. Henriksen-Lacey, D. Jimenez de Aberasturi, A. Sánchez-Iglesias and L. M. Liz-Marzán, *Chem. Mater.*, 2020, **32**, 5879–5889.
- 111 Z. A. Nima, M. Mahmood, Y. Xu, T. Mustafa, F. Watanabe, D. A. Nedosekin, M. A. Juratli, T. Fahmi, E. I. Galanzha, J. P. Nolan, A. G. Basnakian, V. P. Zharov and A. S. Biris, *Sci. Rep.*, 2014, **4**, 4752.
- 112 J. Yang, Z. Wang, S. Zong, C. Song, R. Zhang and Y. Cui, *Anal. Bioanal. Chem.*, 2012, **402**, 1093–1100.
- 113 S. Rodal-Cedeira, A. Vázquez-Arias, G. Bodelón, A. Skorikov, S. Núñez-Sánchez, A. Laporta, L. Polavarapu, S. Bals, L. M. Liz-Marzán, J. Pérez-Juste and I. Pastoriza-Santos, *ACS Nano*, 2020, **14**, 14655–14664.
- 114 S. Barua and S. Mitragotri, *Nano Today*, 2014, **9**, 223–243.
- 115 J. Yue, T. J. Feliciano, W. Li, A. Lee and T. W. Odom, *Bioconjugate Chem.*, 2017, **28**, 1791–1800.
- 116 M. Bhamidipati and L. Fabris, *Bioconjugate Chem.*, 2017, **28**, 449–460.
- 117 P. T. Sujai, M. M. Joseph, G. Saranya, J. B. Nair, V. P. Murali and K. K. Maiti, *Nanoscale*, 2020, **12**, 6971–6975.
- 118 S. M. McCabe, G. Q. Wallace, S. Sloan-Dennison, W. J. Tipping, N. C. Shand, D. Graham, M. Boyd and K. Faulds, *Analyst*, 2023, **148**, 3247–3256.
- 119 A. Kapara, K. A. Findlay Paterson, V. G. Brunton, D. Graham, M. Zagnoni and K. Faulds, *Anal. Chem.*, 2021, **93**, 5862–5871.
- 120 L. E. Jamieson, V. L. Camus, P. O. Bagnaninchi, K. M. Fisher, G. D. Stewart, W. H. Nailon, D. B. McLaren, D. J. Harrison and C. J. Campbell, *Nanoscale*, 2016, **8**, 16710–16718.
- 121 E. J. Zeman and G. C. Schatz, in *Dynamics on Surfaces*, ed. B. Pullman, J. Jortner, A. Nitzan and B. Gerber, Springer, Netherlands, Dordrecht, 1984, vol. 17, pp. 413–424.
- 122 M. Bhamidipati and L. Fabris, *Bioconjugate Chem.*, 2017, **28**, 449–460.
- 123 P. Lavrador, M. R. Esteves, V. M. Gaspar and J. F. Mano, *Adv. Funct. Mater.*, 2021, **31**, 2005941.
- 124 P. Thoniyot, M. J. Tan, A. A. Karim, D. J. Young and X. J. Loh, *Adv. Sci.*, 2015, **2**, 1400010.
- 125 C. Wang, N. T. Flynn and R. Langer, *Adv. Mater.*, 2004, **16**, 1074–1079.
- 126 R. Contreras-Montoya, A. B. Bonhome-Espinosa, A. Orte, D. Miguel, J. M. Delgado-López, J. D. G. Duran, J. M. Cuerva, M. T. Lopez-Lopez and L. Álvarez De Cienfuegos, *Mater. Chem. Front.*, 2018, **2**, 686–699.
- 127 S. E. Lehman, J. M. McCracken, L. A. Miller, S. Jayalath and R. G. Nuzzo, *Adv. Healthcare Mater.*, 2021, **10**, 2001040.
- 128 Y. Tsuge, T. Moriya, Y. Moriyama, Y. Tokura and S. Shiratori, *ACS Appl. Mater. Interfaces*, 2017, **9**, 15122–15129.
- 129 H. Kang, S. Jeong, Y. Park, J. Yim, B. Jun, S. Kyeong, J. Yang, G. Kim, S. Hong, L. P. Lee, J. Kim, H. Lee, D. H. Jeong and Y. Lee, *Adv. Funct. Mater.*, 2013, **23**, 3719–3727.
- 130 K. Zhang, C. Hao, Y. Huo, B. Man, C. Zhang, C. Yang, M. Liu and C. Chen, *Lasers Med. Sci.*, 2019, **34**, 1849–1855.
- 131 S. Mosca, P. Dey, T. A. Tabish, F. Palombo, N. Stone and P. Matousek, *J. Biophotonics*, 2020, **13**, e201960092.
- 132 Y. Zhang, R. Chen, F. Liu, P. Miao, L. Lin and J. Ye, *Small Methods*, 2023, **7**, 2201334.
- 133 D. A. Stuart, J. M. Yuen, N. Shah, O. Lyandres, C. R. Yonzon, M. R. Glucksberg, J. T. Walsh and R. P. Van Duyne, *Anal. Chem.*, 2006, **78**, 7211–7215.
- 134 H. Kang, S. Jeong, Y. Park, J. Yim, B. Jun, S. Kyeong, J. Yang, G. Kim, S. Hong and L. P. Lee, *Adv. Funct. Mater.*, 2013, **23**, 3719–3727.
- 135 H. Maeda, J. Wu, T. Sawa, Y. Matsumura and K. Hori, *J. Controlled Release*, 2000, **65**, 271–284.
- 136 R. M. Davis, B. Kiss, D. R. Trivedi, T. J. Metzner, J. C. Liao and S. S. Gambhir, *ACS Nano*, 2018, **12**, 9669–9679.
- 137 H. Chen, W. Zhang, G. Zhu, J. Xie and X. Chen, *Nat. Rev. Mater.*, 2017, **2**, 17024.
- 138 J. Wang, D. Liang, Q. Jin, J. Feng and X. Tang, *Bioconjugate Chem.*, 2020, **31**, 182–193.
- 139 J. Wang, D. Liang, J. Feng and X. Tang, *Anal. Chem.*, 2019, **91**, 11045–11054.
- 140 A. M. Fales, H. Yuan and T. Vo-Dinh, *Mol. Pharmaceutics*, 2013, **10**, 2291–2298.
- 141 S. McAughtrie, K. Lau, K. Faulds and D. Graham, *Chem. Sci.*, 2013, **4**, 3566.
- 142 E. Lenzi, L. Litti, D. Jimenez de Aberasturi, M. Henriksen-Lacey and L. M. Liz-Marzán, *J. Raman Spectrosc.*, 2021, **52**, 355–365.
- 143 Y. Chen, X. Bai, L. Su, Z. Du, A. Shen, A. Materny and J. Hu, *Sci. Rep.*, 2016, **6**, 19173.
- 144 C. Liu, J. Dong, Z. Zhang, K. Fu, D. Wang, X. Mi, S. Yue, X. Tan and Y. Zhang, *Anal. Chem.*, 2023, **95**, 13880–13888.
- 145 L. A. Dykman and N. G. Khlebtsov, *Chem. Rev.*, 2014, **114**, 1258–1288.
- 146 B. D. Chithrani and W. C. W. Chan, *Nano Lett.*, 2007, **7**, 1542–1550.
- 147 X.-T. Pan, X.-Y. Yang, T.-Q. Mao, K. Liu, Z.-Z. Chen, L.-N. Ji, D.-C. Jiang, K. Wang, Z.-Z. Gu and X.-H. Xia, *Biosensors*, 2022, **12**, 875.
- 148 L. Fang, X.-T. Pan, K. Liu, D. Jiang, D. Ye, L.-N. Ji, K. Wang and X.-H. Xia, *ACS Appl. Mater. Interfaces*, 2023, **15**, 20677–20685.
- 149 S. Vantasin, W. Ji, Y. Tanaka, Y. Kitahama, M. Wang, K. Wongravee, H. Gatemala, S. Ekgasit and Y. Ozaki, *Angew. Chem.*, 2016, **128**, 8531–8535.
- 150 A. Chakraborty, A. Ghosh and A. Barui, *J. Raman Spectrosc.*, 2020, **51**, 7–36.
- 151 J. V. Jokerst, A. J. Cole, D. Van de Sompel and S. S. Gambhir, *ACS Nano*, 2012, **6**, 10366–10377.
- 152 A. M. Mohs, M. C. Mancini, S. Singhal, J. M. Provenzale, B. Leyland-Jones, M. D. Wang and S. Nie, *Anal. Chem.*, 2010, **82**, 9058–9065.
- 153 L. Li, R. Jiang, B. Shan, Y. Lu, C. Zheng and M. Li, *Nat. Commun.*, 2022, **13**, 5249.
- 154 P. Wang, Y. Fan, L. Lu, L. Liu, L. Fan, M. Zhao, Y. Xie, C. Xu and F. Zhang, *Nat. Commun.*, 2018, **9**, 2898.
- 155 H. Karabeber, R. Huang, P. Iacono, J. M. Samii, K. Pitter, E. C. Holland and M. F. Kircher, *ACS Nano*, 2014, **8**, 9755–9766.



- 156 Y. Wen, V. X. Truong and M. Li, *Nano Lett.*, 2021, **21**, 3066–3074.
- 157 L. A. Lane, R. Xue and S. Nie, *Curr. Opin. Chem. Biol.*, 2018, **45**, 95–103.
- 158 H. He, Y. Zhang, S. Zhu, J. Ye and L. Lin, *J. Phys. Chem. C*, 2022, **126**, 12575–12581.
- 159 S. Lin, Z. Cheng, Q. Li, R. Wang and F. Yu, *ACS Sens.*, 2021, **6**, 3912–3932.
- 160 Y. Liu, J. R. Ashton, E. J. Moding, H. Yuan, J. K. Register, A. M. Fales, J. Choi, M. J. Whitley, X. Zhao, Y. Qi, Y. Ma, G. Vaidyanathan, M. R. Zalutsky, D. G. Kirsch, C. T. Badea and T. Vo-Dinh, *Theranostics*, 2015, **5**, 946–960.
- 161 C. De La Encarnación, D. Jimenez De Aberasturi and L. M. Liz-Marzán, *Adv. Drug Delivery Rev.*, 2022, **189**, 114484.
- 162 M. Quintanilla, Y. Zhang and L. M. Liz-Marzán, *Chem. Mater.*, 2018, **30**, 2819–2828.
- 163 M. Quintanilla, M. Henriksen-Lacey, C. Renero-Lecuna and L. M. Liz-Marzán, *Chem. Soc. Rev.*, 2022, **51**, 4223–4242.
- 164 M. Quintanilla, I. García, I. De Lázaro, R. García-Alvarez, M. Henriksen-Lacey, S. Vranic, K. Kostarelos and L. M. Liz-Marzán, *Theranostics*, 2019, **9**, 7298–7312.
- 165 D.-E. Lee, H. Koo, I.-C. Sun, J. H. Ryu, K. Kim and I. C. Kwon, *Chem. Soc. Rev.*, 2012, **41**, 2656–2672.
- 166 Z. Wang, S. Zong, J. Yang, J. Li and Y. Cui, *Biosens. Bioelectron.*, 2011, **26**, 2883–2889.
- 167 S. Lee, H. Chon, S.-Y. Yoon, E. K. Lee, S.-I. Chang, D. W. Lim and J. Choo, *Nanoscale*, 2012, **4**, 124–129.
- 168 A. B. Serrano-Montes, J. Langer, M. Henriksen-Lacey, D. Jimenez de Aberasturi, D. M. Solís, J. M. Taboada, F. Obelleiro, K. Sentosun, S. Bals, A. Bekdemir, F. Stellacci and L. M. Liz-Marzán, *J. Phys. Chem. C*, 2016, **120**, 20860–20868.
- 169 M. S. Strozyk, D. J. de Aberasturi, J. V. Gregory, M. Brust, J. Lahann and L. M. Liz-Marzán, *Adv. Funct. Mater.*, 2017, **27**, 1701626.
- 170 E. Lenzi, D. Jimenez de Aberasturi, M. Henriksen-Lacey, P. Piñeiro, A. J. Muniz, J. Lahann and L. M. Liz-Marzán, *ACS Appl. Mater. Interfaces*, 2022, **14**, 20708–20719.
- 171 J. Qian, L. Jiang, F. Cai, D. Wang and S. He, *Biomaterials*, 2011, **32**, 1601–1610.
- 172 Y. Zhang, J. Qian, D. Wang, Y. Wang and S. He, *Angew. Chem., Int. Ed.*, 2013, **52**, 1148–1151.
- 173 Y. Zhang, H. Liu, J. Tang, Z. Li, X. Zhou, R. Zhang, L. Chen, Y. Mao and C. Li, *ACS Appl. Mater. Interfaces*, 2017, **9**, 17769–17776.
- 174 A. A. Stacy and R. P. Van Duyne, *Chem. Phys. Lett.*, 1983, **102**, 365–370.
- 175 S. Harmsen, R. Huang, M. A. Wall, H. Karabeber, J. M. Samii, M. Spaliviero, J. R. White, S. Monette, R. O'Connor, K. L. Pitter, S. A. Sastra, M. Saborowski, E. C. Holland, S. Singer, K. P. Olive, S. W. Lowe, R. G. Blasberg and M. F. Kircher, *Sci. Transl. Med.*, 2015, **7**, 271ra7–271ra7.
- 176 V. Neuschmelting, S. Harmsen, N. Beziere, H. Lockau, H.-T. Hsu, R. Huang, D. Razansky, V. Ntziachristos and M. F. Kircher, *Small*, 2018, **14**, 1800740.
- 177 D. Graham, W. E. Smith, A. M. T. Linacre, C. H. Munro, N. D. Watson and P. C. White, *Anal. Chem.*, 1997, **69**, 4703–4707.
- 178 R. J. Stokes, A. Macaskill, J. A. Dougan, P. G. Hargreaves, H. M. Stanford, W. E. Smith, K. Faulds and D. Graham, *Chem. Commun.*, 2007, 2811–2813.
- 179 A. Ingram, L. Byers, K. Faulds, B. D. Moore and D. Graham, *J. Am. Chem. Soc.*, 2008, **130**, 11846–11847.
- 180 H. Cho, B. R. Baker, S. Wachsmann-Hogiu, C. V. Pagba, T. A. Laurence, S. M. Lane, L. P. Lee and J. B.-H. Tok, *Nano Lett.*, 2008, **8**, 4386–4390.
- 181 G. Sabatté, R. Keir, M. Lawlor, M. Black, D. Graham and W. E. Smith, *Anal. Chem.*, 2008, **80**, 2351–2356.
- 182 G. McNay, D. Eustace, W. E. Smith, K. Faulds and D. Graham, *Appl. Spectrosc.*, 2011, **65**, 825–837.
- 183 Y. Zhang, D. Jimenez De Aberasturi, M. Henriksen-Lacey, J. Langer and L. M. Liz-Marzán, *ACS Sens.*, 2020, **5**, 3194–3206.
- 184 R. A. Ando, N. P. W. Pieczonka, P. S. Santos and R. F. Aroca, *Phys. Chem. Chem. Phys.*, 2009, **11**, 7505.
- 185 X. Zou, Y. Wang, W. Liu and L. Chen, *Analyst*, 2017, **142**, 2333–2337.
- 186 S. Kang, W. Nam, W. Zhou, I. Kim and P. J. Vikesland, *ACS Appl. Nano Mater.*, 2021, **4**, 5768–5777.
- 187 F. Madzharova, Z. Heiner and J. Kneipp, *Chem. Soc. Rev.*, 2017, **46**, 3980–3999.
- 188 S. Mosca, P. Dey, M. Salimi, B. Gardner, F. Palombo, N. Stone and P. Matousek, *Anal. Chem.*, 2021, **93**, 6755–6762.
- 189 N. Stone, K. Faulds, D. Graham and P. Matousek, *Anal. Chem.*, 2010, **82**, 3969–3973.
- 190 S. N. K. M. L. GR, *Chem. Sci.*, 2011, **2**, 776–780.
- 191 P. Matousek, M. D. Morris, N. Everall, I. P. Clark, M. Towrie, E. Draper, A. Goodship and A. W. Parker, *Appl. Spectrosc.*, 2005, **59**, 1485–1492.
- 192 S. M. Asiala, N. C. Shand, K. Faulds and D. Graham, *ACS Appl. Mater. Interfaces*, 2017, **9**, 25488–25494.
- 193 B. Sharma, K. Ma, M. R. Glucksberg and R. P. Van Duyne, *J. Am. Chem. Soc.*, 2013, **135**, 17290–17293.
- 194 A. S. Moody, P. C. Baghernejad, K. R. Webb and B. Sharma, *Anal. Chem.*, 2017, **89**, 5688–5692.
- 195 R. A. Odion, P. Strobbia, B. M. Crawford and T. Vo-Dinh, *J. Raman Spectrosc.*, 2018, **49**, 1452–1460.
- 196 F. Nicolson, L. E. Jamieson, S. Mabbott, K. Plakas, N. C. Shand, M. R. Detty, D. Graham and K. Faulds, *Chem. Commun.*, 2018, **54**, 8530–8533.
- 197 F. Nicolson, B. Andreiuk, C. Andreou, H.-T. Hsu, S. Rudder and M. F. Kircher, *Theranostics*, 2019, **9**, 5899.
- 198 Y. Kitahama and Y. Ozaki, *Analyst*, 2016, **141**, 5020–5036.
- 199 S. Mosca, C. Conti, N. Stone and P. Matousek, *Nat. Rev. Methods Primers*, 2021, **1**, 21.
- 200 S. Tanwar, K. K. Haldar and T. Sen, *J. Am. Chem. Soc.*, 2017, **139**, 17639–17648.
- 201 M. Bhamidipati, H.-Y. Cho, K.-B. Lee and L. Fabris, *Bioconjugate Chem.*, 2018, **29**, 2970–2981.
- 202 S. C.-H. Tsao, J. Wang, Y. Wang, A. Behren, J. Cebon and M. Trau, *Nat. Commun.*, 2018, **9**, 1482.
- 203 S. Cervo, E. Mansutti, G. Del Mistro, R. Spizzo, A. Colombatti, A. Steffan, V. Sergio and A. Bonifacio, *Anal. Bioanal. Chem.*, 2015, **407**, 7503–7509.



- 204 A. Stefancu, V. Moisoiu, R. Couti, I. Andras, R. Rahota, D. Crisan, I. E. Pavel, C. Socaciu, N. Leopold and N. Crisan, *Nanomedicine*, 2018, **13**, 2455–2467.
- 205 L. Shi, Y. Li and Z. Li, *Light: Sci. Appl.*, 2023, **12**, 234.
- 206 J. Hoarau-Véchet, A. Raffi, C. Touboul and J. Pasquier, *Int. J. Mol. Sci.*, 2018, **19**, 181.
- 207 J. Folkman, *Nat. Med.*, 1995, **1**, 27–30.
- 208 Z. Qian, J. Fei, S. Zong, K. Yang, L. Li, R. Liu, Z. Wang and Y. Cui, *ACS Sens.*, 2020, **5**, 208–216.
- 209 A. Antignani, E. C. H. Ho, M. T. Bilotta, R. Qiu, R. Sarnvosky and D. J. FitzGerald, *Biomolecules*, 2020, **10**, 1331.
- 210 M. Brisset, M. Grandin, A. Bernet, P. Mehlen and F. Hollande, *EMBO Mol. Med.*, 2021, **13**, e14495.
- 211 A. Samanta, K. K. Maiti, K. Soh, X. Liao, M. Vendrell, U. Dinish, S. Yun, R. Bhuvanewari, H. Kim and S. Rautela, *Angew. Chem., Int. Ed.*, 2011, **50**, 6089.
- 212 U. S. Dinish, G. Balasundaram, Y.-T. Chang and M. Olivo, *Sci. Rep.*, 2014, **4**, 4075.
- 213 M. Altunbek, D. Çetin, Z. Suludere and M. Çulha, *Talanta*, 2019, **191**, 390–399.
- 214 J. Plou, P. S. Valera, I. García, C. D. L. De Albuquerque, A. Carracedo and L. M. Liz-Marzán, *ACS Photonics*, 2022, **9**, 333–350.
- 215 L. Zeng, Y. Pan, S. Wang, X. Wang, X. Zhao, W. Ren, G. Lu and A. Wu, *ACS Appl. Mater. Interfaces*, 2015, **7**, 16781–16791.
- 216 B. Yin, W. K. H. Ho, X. Xia, C. K. W. Chan, Q. Zhang, Y. M. Ng, C. Y. K. Lam, J. C. W. Cheung, J. Wang and M. Yang, *Small*, 2023, **19**, 2206762.
- 217 D. Lagadic-Gossmann, L. Huc and V. Lecureur, *Cell Death Differ.*, 2004, **11**, 953–961.
- 218 S. Gilles, C. Kaulen, M. Pabst, U. Simon, A. Offenhäusser and D. Mayer, *Nanotechnology*, 2011, **22**, 295301.
- 219 M. T. Ghoneim, A. Nguyen, N. Dereje, J. Huang, G. C. Moore, P. J. Murzynowski and C. Dagdeviren, *Chem. Rev.*, 2019, **119**, 5248–5297.
- 220 M. Aref, E. Ranjbari, J. J. García-Guzmán, K. Hu, A. Lork, G. A. Crespo, A. G. Ewing and M. Cuartero, *Anal. Chem.*, 2021, **93**, 15744–15751.
- 221 J. Guo, A. Sesena Rubfiaro, Y. Lai, J. Moscoso, F. Chen, Y. Liu, X. Wang and J. He, *Analyst*, 2020, **145**, 4852–4859.
- 222 B. P. Nadappuram, K. McKelvey, R. Al Botros, A. W. Colburn and P. R. Unwin, *Anal. Chem.*, 2013, **85**, 8070–8074.
- 223 H. T. Phan and A. J. Haes, *J. Phys. Chem. C*, 2018, **122**, 14846–14856.
- 224 K. Sokołowska, S. Malola, M. Lahtinen, V. Saarnio, P. Permi, K. Koskinen, M. Jalasvuori, H. Häkkinen, L. Lehtovaara and T. Lahtinen, *J. Phys. Chem. C*, 2019, **123**, 2602–2612.
- 225 Y. Zhang, I. Gallego, J. Plou, J. L. Pedraz, L. M. Liz-Marzán, J. Ciriza and I. García, *Nanoscale*, 2021, **13**, 14354–14362.
- 226 J. Kneipp, H. Kneipp, B. Wittig and K. Kneipp, *Nano Lett.*, 2007, **7**, 2819–2823.
- 227 X.-S. Zheng, P. Hu, Y. Cui, C. Zong, J.-M. Feng, X. Wang and B. Ren, *Anal. Chem.*, 2014, **86**, 12250–12257.
- 228 A. Capocefalo, D. Mammucari, F. Brasili, C. Fasolato, F. Bordi, P. Postorino and F. Domenici, *Front. Chem.*, 2019, **7**, 413.
- 229 Z. Zhang, K. Bando, K. Mochizuki, A. Taguchi, K. Fujita and S. Kawata, *Anal. Chem.*, 2019, **91**, 3254–3262.
- 230 M. Xu, X. Ma, T. Wei, Z.-X. Lu and B. Ren, *Anal. Chem.*, 2018, **90**, 13922–13928.
- 231 L. E. Jamieson, D. J. Harrison and C. J. Campbell, *Analyst*, 2015, **140**, 3910–3920.
- 232 W. H. Skinner, N. Robinson, G. R. Hardisty, H. Fleming, A. Geddis, M. Bradley, R. D. Gray and C. J. Campbell, *Chem. Commun.*, 2023, **59**, 3249–3252.
- 233 A. Williams, K. J. Flynn, Z. Xia and P. R. Dunstan, *J. Raman Spectrosc.*, 2016, **47**, 819–827.
- 234 S. Kang, W. Nam, W. Zhou, I. Kim and P. J. Vikesland, *ACS Appl. Nano Mater.*, 2021, **4**, 5768–5777.
- 235 J. Plou, P. S. Valera, I. García, D. Vila-Liarte, C. Renero-Lecuna, J. Ruiz-Cabello, A. Carracedo and L. M. Liz-Marzán, *Small*, 2023, 2207658.
- 236 N. M. Ralbovsky and I. K. Lednev, *Chem. Soc. Rev.*, 2020, **49**, 7428–7453.
- 237 S. Đorđević, M. M. Gonzalez, I. Conejos-Sánchez, B. Carreira, S. Pozzi, R. C. Acúrcio, R. Satchi-Fainaro, H. F. Florindo and M. J. Vicent, *Drug Delivery Transl. Res.*, 2022, **12**, 500–525.
- 238 D. Bobo, K. J. Robinson, J. Islam, K. J. Thurecht and S. R. Corrie, *Pharm. Res.*, 2016, **33**, 2373–2387.
- 239 R. Zhang, F. Kiessling, T. Lammers and R. M. Pallares, *Drug Delivery Transl. Res.*, 2023, **13**, 378–385.
- 240 J. Jehlička and A. Culka, *Anal. Chim. Acta*, 2022, **1209**, 339027.
- 241 I. A. Bratchenko, L. A. Bratchenko, A. A. Moryatov, Y. A. Khristoforova, D. N. Artemyev, O. O. Myakinin, A. E. Orlov, S. V. Kozlov and V. P. Zakharov, *Exp. Dermatol.*, 2021, **30**, 652–663.
- 242 E. Garai, S. Sensarn, C. L. Zavaleta, N. O. Loewke, S. Rogalla, M. J. Mandella, S. A. Felt, S. Friedland, J. T. C. Liu, S. S. Gambhir and C. H. Contag, *PLoS One*, 2015, **10**, e0123185.
- 243 A. Kamińska, E. Witkowska, A. Kowalska, A. Skoczyńska, P. Ronkiewicz, T. Szymborski and J. Waluk, *Anal. Methods*, 2016, **8**, 4521–4529.
- 244 X.-S. Zheng, I. J. Jahn, K. Weber, D. Cialla-May and J. Popp, *Spectrochim. Acta, Part A*, 2018, **197**, 56–77.
- 245 X. Huang, B. Sheng, H. Tian, Q. Chen, Y. Yang, B. Bui, J. Pi, H. Cai, S. Chen, J. Zhang, W. Chen, H. Zhou and P. Sun, *Acta Pharm. Sin. B*, 2023, **13**, 1303–1317.
- 246 P. Wang, M. Xia, O. Liang, K. Sun, A. F. Cipriano, T. Schroeder, H. Liu and Y.-H. Xie, *Anal. Chem.*, 2015, **87**, 10255–10261.
- 247 X. X. Han, B. Zhao and Y. Ozaki, *Anal. Bioanal. Chem.*, 2009, **394**, 1719–1727.
- 248 S. Laing, K. Gracie and K. Faulds, *Chem. Soc. Rev.*, 2016, **45**, 1901–1918.
- 249 J. Plou, I. García, M. Charconnet, I. Astobiza, C. García-Astrain, C. Matricardi, A. Mihi, A. Carracedo and L. M. Liz-Marzán, *Adv. Funct. Mater.*, 2020, **30**, 1910335.
- 250 M. I. Anik, A. Pan, M. G. Jakaria, S. A. Meenach and G. D. Bothun, *ACS Appl. Nano Mater.*, 2022, **5**, 14356–14366.
- 251 S. Lin, H. Ze, X. Zhang, Y. Zhang, J. Song, H. Zhang, H. Zhong, Z. Yang, C. Yang and J. Li, *Angew. Chem., Int. Ed.*, 2022, **61**, e202203511.



- 252 T. Kang, S. M. Yoo, I. Yoon, S. Y. Lee and B. Kim, *Nano Lett.*, 2010, **10**, 1189–1193.
- 253 Y. Wang, S. Rauf, Y. S. Grewal, L. J. Spadafora, M. J. A. Shiddiky, G. A. Cangelosi, S. Schlücker and M. Trau, *Anal. Chem.*, 2014, **86**, 9930–9938.
- 254 Y. Zhan, R. Fei, Y. Lu, Y. Wan, X. Wu, J. Dong, D. Meng, Q. Ge and X. Zhao, *Analyst*, 2022, **147**, 4124–4131.
- 255 I. Badillo-Ramírez, B. Landeros-Rivera, J. M. Saniger, J. Popp and D. Cialla-May, *Analyst*, 2023, **148**, 1848–1857.
- 256 J. E. L. Villa, I. Garcia, D. Jimenez de Aberasturi, V. Pavlov, M. D. P. T. Sotomayor and L. M. Liz-Marzán, *Biosens. Bioelectron.*, 2020, **165**, 112418.
- 257 B. Tadgell and L. M. Liz-Marzán, *Chem. – Eur. J.*, 2023, e202301691.

